1

The MESSENGER Mission: Science and Implementation Overview

SEAN C. SOLOMON AND BRIAN J. ANDERSON

1.1 INTRODUCTION

Although a sibling of Earth, Venus, and Mars, the planet Mercury is an unusual member of the family (Solomon, 2003). Among the planets of our solar system, it is the smallest, at little more than 5% of an Earth mass, but its bulk density corrected for the effect of internal compression is the highest. Mercury's orbit is the most eccentric of the planets, and it is the only known solar system object in a 3:2 spin–orbit resonance, in which three sidereal days equal two periods of Mercury's revolution about the Sun. Mercury is the only inner planet other than Earth to host an internal magnetic field and an Earth-like magnetosphere capable of standing off the solar wind. The closest planet to the Sun, Mercury experiences a variation in surface temperature at the equator of 600°C over the course of a solar day, which because of Mercury's slow spin rate equals two Mercury years. The permanently shadowed floors of Mercury's high-latitude craters nonetheless are sufficiently cold to have trapped water ice and other frozen volatiles.

Thought to have been created by the same processes as the other inner planets and at the same early stage in the history of the solar system, Mercury with its unusual attributes has long held out the promise of deepening our understanding of how Earth and other Earth-like planets formed and evolved. Yet Mercury is not an easy object to study. Never separated from the Sun by more than 28° of arc when viewed from Earth, Mercury is forbidden as a target for the Hubble Space Telescope and other astronomical facilities because their optical systems would be severely damaged by exposure to direct sunlight. Located deep within the gravitational potential well of the Sun, Mercury has also long presented a challenge to spacecraft mission design. The first spacecraft to view Mercury at close range was Mariner 10, which after flying once by Venus encountered the innermost planet three times in 1974–1975. The encounters occurred nearly at Mercury's greatest distance from the Sun and were spaced approximately one Mercury solar day apart, so the same hemisphere of the planet was in sunlight at each flyby. Mariner 10 obtained images of 45% of the surface, discovered the planet's global magnetic field, assayed three neutral species (H, He, and O) in Mercury's tenuous atmosphere, and sampled the magnetic field and energetic charged particles in Mercury's dynamic magnetosphere (Dunne and Burgess, 1978).

After the Mariner 10 mission, the next logical step in the exploration of Mercury was widely viewed to be an orbiter mission (COMPLEX, 1978), and several notable discoveries by ground-based astronomers in the years since the Mariner 10 encounters (e.g., Potter and Morgan, 1985, 1986; Slade et al., 1992; Harmon and Slade, 1992) provided a wealth of new information about Mercury that whetted the appetite of the planetary science community for orbital observations. Nevertheless, substantial advances were needed in mission design, thermal engineering, and miniaturization of instruments and spacecraft subsystems before such a mission could be considered technically ready.

The MErcury Surface, Space ENvironment, GEochemistry, and Ranging (MESSENGER) mission to orbit Mercury was proposed under NASA's Discovery Program in 1996 and again in 1998 (Solomon et al., 2001; Gold et al., 2001; Santo et al., 2001) and was selected for flight in 1999. Development, construction, integration, and testing of the spacecraft and its instruments began in January 2000 and spanned the four and a half years leading to launch on 3 August 2004 (McNutt et al., 2006). MESSENGER completed gravity-assist flybys of Earth once, Venus twice, and Mercury three times (Figure 1.1) during a mission cruise phase that lasted 6.6 years. MESSENGER was inserted into orbit about Mercury on 18 March 2011 and conducted orbital observations of the innermost planet for more than four years, until 30 April 2015.

In this chapter we provide an overview of the MESSENGER mission from a historical perspective, including the mission's scientific objectives; the payload characteristics, data acquisition planning, and operational procedures adopted to achieve those objectives; and the scientific findings from flyby and orbital operations. We begin with summaries of the mission objectives, spacecraft, payload instruments, and orbit design. We then describe the procedures adopted to optimize the scientific return from the complex series of orbital data acquisition operations. We follow with an account of the primary mission, including the Mercury flybys and the first year of orbital observations. We then outline the rationale for and accomplishments of MESSENGER's first extended mission, conducted over the second year of orbital operations, and the second extended mission, conducted over the final two years of orbital operations. The second extended mission included a distinctive low-altitude campaign completed at the culmination of the mission. A concluding section briefly introduces the other chapters of this book.

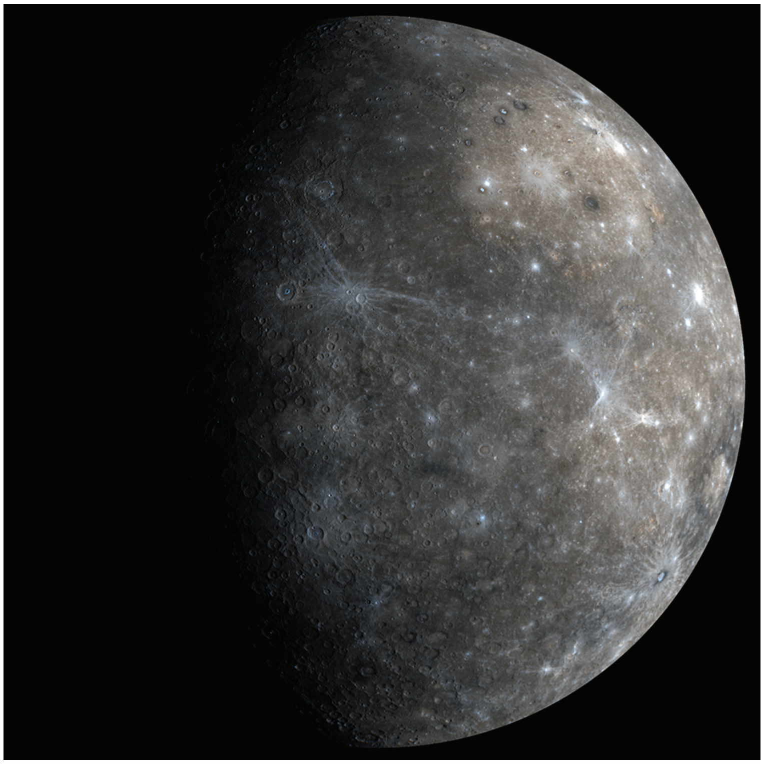

Figure 1.1. Image mosaic of Mercury acquired on departure from MESSENGER's first Mercury flyby on 14 January 2008. Mercury Dual Imaging System wide-angle camera images acquired through the narrow-band filters centered at 1000, 700, and 430 nm are projected in red, green, and blue in this color representation. Much of the area shown had not been imaged by Mariner 10.

1.2 MISSION OBJECTIVES, SPACECRAFT, PAYLOAD, AND ORBIT DESIGN

1.2.1 Key Scientific Questions

The MESSENGER mission was designed to address six key scientific questions. The questions were motivated by the knowledge of Mercury available at the time the mission was proposed, were capable of being substantially addressed by measurements that could be made from orbit, and would yield answers that would bear not only on the nature of Mercury but more generally on the origin and comparative evolution of the inner planets as a group. Those questions and a brief summary of the rationale for each were as follows.

1.2.1.1 What Planetary Formational Processes Led to the High Ratio of Metal to Silicate in Mercury?

The Mariner 10 spacecraft carried no elemental remote sensing instruments, so at the time the MESSENGER mission was proposed the single most important piece of information about the planet's bulk composition was its high uncompressed density, which implied that Mercury has an iron-rich core that occupies much higher fractions of the planet's mass and volume than do the cores of the other inner planets (e.g., Siegfried and Solomon, 1974). A variety of theories for the origin and early evolution of Mercury had been advanced to account for its high metal fraction, including formation from metal-enriched precursors resulting from either high-temperature fractionation or aerodynamical sorting in the solar nebula (e.g., Weidenschilling, 1978; Lewis, 1988) or removal of an initially larger silicate crust and mantle by evaporation or giant impact (e.g., Cameron, 1985; Wetherill, 1988; Benz et al., 1988). Those theories differed in their predictions for the bulk composition of the silicate fraction of the planet (e.g., Lewis, 1988), including the upper crust, which would be visible to geochemical remote sensing instruments on an orbiting spacecraft. Moreover, ground-based telescopic measurements of Mercury's surface reflectance showed few if any absorption features commonly seen in reflectance spectra of the Moon, Mars, and asteroids and attributable to the presence of ferrous iron in silicate minerals (e.g., Vilas, 1988), indicating both a low abundance of ferrous iron on Mercury's surface and the need to rely heavily on elemental remote sensing instruments to gain compositional information.

1.2.1.2 What Is the Geological History of Mercury?

Because of Mercury's size, intermediate between the Moon and Mars, as well as its high metal/silicate ratio, documenting the geological history of Mercury was viewed as crucial to understanding how terrestrial planet evolution depends on planet size and initial conditions. A broad geological history of Mercury had been developed from Mariner 10 images (e.g., Strom, 1979; Spudis and Guest, 1988), but the limited coverage and resolution of those images left many aspects of that history uncertain. Extensive plains units were documented by Mariner 10, and the youngest of those plains deposits were seen to be in stratigraphic positions similar to the volcanic lunar maria. Unlike the maria, however, the plains deposits on Mercury are not markedly lower in reflectance than the surrounding older terrain, and no volcanic landforms were visible at the resolution of Mariner 10 images, so both volcanic and impact ejecta processes for plains emplacement had been suggested (e.g., Strom et al., 1975; Wilhelms,

1976) and the importance of volcanism in Mercury's history was thus uncertain. Deformational features on Mercury were seen to be dominantly contractional, leading to the proposal that such features were the expression of global contraction resulting from interior cooling (e.g., Strom et al., 1975), although the restricted imaging coverage meant that the global contraction hypothesis remained untested over slightly more than a full hemisphere of the planet.

1.2.1.3 What Are the Nature and Origin of Mercury's Magnetic Field?

Measurements by Mariner 10 demonstrated that Mercury has an internal magnetic field (Ness et al., 1976) with a dipole component nearly orthogonal to the planet's orbital plane and an estimated moment near 300 nT R_M^3, where R_M is Mercury's mean radius (Connerney and Ness, 1988). Because external sources can dominate the total field measured at Mercury, and because of the limited sampling of the field during the two Mariner 10 flybys that penetrated Mercury's magnetosphere, the uncertainty in Mercury's dipole moment derived from Mariner 10 data was a factor of 2, and higher-order terms were linearly dependent and thus not resolvable (Connerney and Ness, 1988). A variety of mechanisms for producing Mercury's observed magnetic field had been proposed, including remanent or fossil fields in Mercury's crust and lithosphere (Stephenson, 1976; Srnka, 1976; Aharonson et al., 2004), hydromagnetic dynamos in a fluid outer core (e.g., Schubert et al., 1988; Stanley et al., 2005; Christensen, 2006), and a thermoelectric dynamo driven by temperature differences along the top of the core (Stevenson, 1987; Giampieri and Balogh, 2002). The different field generation models made different predictions regarding the geometry of the field, particularly for terms of higher order than the dipole term, and so measurements made from orbit about the planet were seen to be needed to distinguish among hypotheses.

1.2.1.4 What Are the Structure and State of Mercury's Core?

The size and physical state of Mercury's core are key to understanding the planet's bulk composition, thermal history, and magnetic field generation processes (Zuber et al., 2007). Peale (1976) realized that the existence and radius of a liquid outer core on Mercury can be determined by the measurement of Mercury's obliquity, the amplitude of its physical libration forced by variations in the torque exerted by the gravitational pull of the Sun over the planet's 88-day orbit period, and two quantities that define the shape of the planet's gravity field at spherical harmonic degree and order 2. The required coefficients in the spherical harmonic expansion of Mercury's gravity field had been estimated from radio tracking of the Mariner 10 flybys (Anderson et al., 1987) but not with high precision. All four quantities can be determined from measurements made by an orbiting spacecraft with sufficient precision to determine Mercury's polar moment of inertia and the moment of inertia of the planet's solid outer shell that participates in the 88-day libration (Peale, 1976: Peale et al., 2002), and from those quantities important aspects of Mercury's internal structure can be resolved. Mercury's obliquity and forced libration amplitude can also be measured from Earth-based radar observations, and such measurements were reported by Margot et al. (2007) before MESSENGER was inserted into orbit around Mercury, and then refined several years later (Margot et al., 2012). Although the measurements of libration amplitude and obliquity indicated that Mercury does indeed possess a fluid outer core (Margot et al., 2007), the uncertainties in Mercury's gravitational field coefficients at harmonic degree 2 dominated the uncertainty in the planet's moments of inertia. Radio tracking of an orbiting spacecraft was required to improve the determination of these key quantities.

1.2.1.5 What Are the Radar-Reflective Materials at Mercury's Poles?

The discovery in 1991 of radar-bright regions near Mercury's poles and the similarity of the radar reflectivity and polarization characteristics of such regions to those of icy satellites and the south residual polar cap of Mars led to the proposal that these areas host deposits of surface or near-surface water ice (Slade et al., 1992; Harmon and Slade, 1992). Subsequent radar imaging at improved resolution confirmed that the radar-bright deposits are confined to the floors of near-polar impact craters (e.g., Harmon et al., 2011). Because of Mercury's small obliquity, sufficiently deep craters are permanently shadowed and are predicted to be at temperatures at which water ice is stable for billions of years (Paige et al., 1992). Although a contribution from interior outgassing could not be excluded, impact volatilization of cometary and meteoritic material followed by transport of water molecules to polar cold traps was shown to provide sufficient polar ice to match the characteristics of the deposits (Moses et al., 1999).

Two alternative explanations for the radar-bright polar deposits of Mercury were nonetheless suggested. One was that the polar deposits are composed of elemental sulfur, on the grounds that sulfur would be stable in polar cold traps and the presence of sulfides in the regolith can account for a high disk-averaged index of refraction and low microwave opacity of surface materials (Sprague et al., 1995). The second was that the permanently shadowed portions of polar craters are radar-bright not because of trapped volatiles but because of either unusual surface roughness (Weidenschilling, 1998) or low dielectric loss (Starukhina, 2001) of near-surface silicates at extremely cold temperatures. Geochemical remote sensing measurements made from orbit around Mercury were recognized as able to distinguish among the competing proposals.

1.2.1.6 What Are the Important Volatile Species and Their Sources and Sinks on and near Mercury?

Mercury's atmosphere is a surface-bounded exosphere for which the composition and behavior are controlled by interactions with the magnetosphere and the surface. At the time the MESSENGER mission was under development, the atmosphere was known to contain at least six elements (H, He, O, Na, K, Ca). The Mariner 10 airglow spectrometer detected H and He and set an upper bound on O (Broadfoot et al., 1976), and ground-based spectroscopic observations led to the discovery of exospheric Na (Potter and Morgan, 1985), K (Potter and Morgan, 1986), and Ca (Bida et al., 2000). Exospheric H and He were thought to be dominated by solar wind ions neutralized by recombination at the surface, whereas proposed source processes for other exospheric species included diffusion from the planet's interior, evaporation, sputtering by photons and energetic ions, chemical sputtering by protons, and meteoroid impact and vaporization (e.g., Killen and Ip, 1999). That several of these processes play some role was suggested by the strong variations in exospheric characteristics observed as functions of local time, solar distance, and level of solar activity (e.g., Sprague et al., 1998; Hunten and Sprague, 2002; Leblanc and Johnson, 2003). It was long recognized that a spacecraft in orbit about Mercury can provide a range of opportunities for elucidating further the nature of the exosphere, through profiles of major exospheric neutral species versus time of day and solar distance and searches for new species (e.g., Domingue et al., 2007). In situ measurement of energetic and thermal plasma ions from orbit can also detect solar wind pickup ions that originated as exospheric neutral atoms (e.g., Koehn et al., 2002).

1.2.2 Scientific Objectives

The six key questions above led to a set of scientific objectives for the MESSENGER mission and in turn to a set of project requirements (Solomon et al., 2001), a suite of payload instruments (Gold et al., 2001), and a measurement strategy (Section 1.3). The scientific objectives for MESSENGER's primary mission are given in Table 1.1, and the project requirements for the primary mission are given in Table 1.2.

The objective to characterize the chemical composition of Mercury's surface led to a project requirement for global maps of major element composition at a resolution sufficient to discern the principal geological units and to distinguish material excavated and ejected by young impact craters from a possible veneer of cometary and meteoritic material. Information on surface mineralogy was also deemed important for this objective. The objective to determine the planet's geological history led to a project requirement for global monochrome imaging at a resolution of hundreds of meters or better, for topographic profiles across key geological features from altimetry or stereo, and for spectral measurements of major geologic units at spatial resolutions of several kilometers or better. The objective to characterize Mercury's magnetic field led to a project requirement for magnetometry, both near the planet and throughout the magnetosphere, as well as for energetic particle and plasma measurements so as to assist in the separation of external and internal fields. The objective to estimate the size and state of Mercury's core led to the project requirement for altimetric measurement of the amplitude of Mercury's physical libration as well as determination of the planet's obliquity and low-degree gravitational field. The objective to assay the volatile inventory at Mercury's poles led to the project requirement for ultraviolet spectrometry of the polar atmosphere and for gamma-ray and neutron spectrometry, imaging, and altimetry of polar-region craters. The objective to characterize the nature of Mercury's exosphere and magnetosphere led to the project requirement to identify all major neutral species in the exosphere and charged species in the magnetosphere.

Table 1.1. *Scientific objectives for MESSENGER's primary mission.*

1. Determine the chemical composition of Mercury's surface.
2. Determine Mercury's geological history.
3. Determine the nature of Mercury's magnetic field.
4. Determine the size and state of Mercury's core.
5. Determine the volatile inventory at Mercury's poles.
6. Determine the nature of Mercury's exosphere and magnetosphere.

1.2.3 Spacecraft

The design of the MESSENGER spacecraft (Figure 1.2) was driven largely by two requirements: to minimize mass and to survive the harsh thermal environment at Mercury (Santo et al., 2001; Leary et al., 2007). The largest launch vehicle available to the Discovery Program was the Delta II 7925-H, which could inject ~1100 kg into the required interplanetary trajectory. Because more than half of that total launch mass was needed for the propellant required to achieve the mission design, only 500 kg remained for the total spacecraft dry mass. To meet this constraint, the spacecraft structure was fabricated primarily with lightweight composite material and was fully integrated with a dual-mode propulsion system that

Table 1.2. *Project requirements for MESSENGER's primary mission.*

1. Provide major-element maps of Mercury to 10% relative uncertainty on the 1000-km scale and determine local composition and mineralogy at the ~20-km scale.

2a. Provide a global map with >90% coverage (monochrome) at 250-m average resolution and >80% of the planet imaged stereoscopically.

2b. Provide a global multispectral map at 2-km/pixel average resolution.

2c. Sample half of the northern hemisphere for topography at 1.5-m average height resolution.

3. Provide a multipole magnetic field model resolved through quadrupole terms with an uncertainty of less than ~20% in the dipole magnitude and direction.

4. Provide a global gravity field to degree and order 16 and determine the ratio of the solid-planet moment of inertia to the total moment of inertia to ~20% or better.

5. Identify the principal component of the radar-reflective material at Mercury's north pole.

6. Provide altitude profiles at 25-km resolution of the major neutral exospheric species and characterize the major ion-species energy distributions as functions of local time, Mercury heliocentric distance, and solar activity.

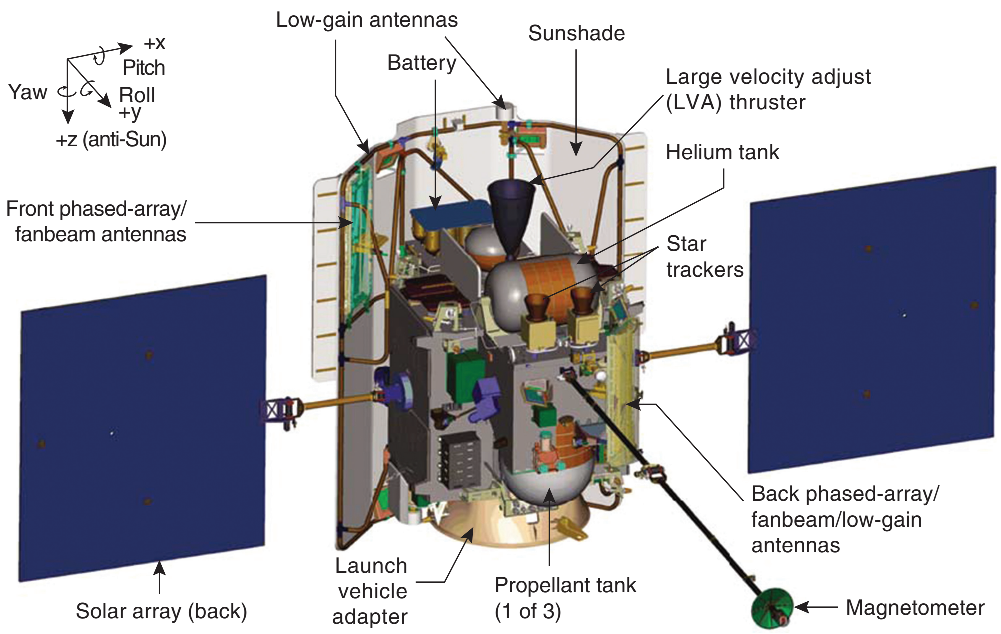

Figure 1.2. Engineering view of the MESSENGER spacecraft from behind the sunshade.

featured lightweight tanks for propellant (hydrazine), oxidizer (nitrous tetroxide), and pressurant (gaseous helium). The propulsion system included a total of 17 thrusters: a single large velocity adjustment bipropellant thruster; four 22-N monopropellant thrusters for thrust-vector steering during large spacecraft maneuvers and for trajectory-correction maneuvers; and 12 4.4-N monopropellant thrusters for attitude control, angular momentum management, and small trajectory-correction maneuvers.

A large number of mass-reduction measures were used in the development of the spacecraft. To avoid a cumbersome gimbaled antenna and the challenges associated with testing and operating it at high temperatures, an electronically steerable phased-array system was developed for the high-gain antenna. Used one at a time, each of two antennas – one on the spacecraft's Sun-facing side and one aft – could be steered about one axis while the spacecraft body rolled about a second axis to point the antenna toward Earth at any point in the mission. The phased-array antennas were complemented with two medium-gain fanbeam antennas and four low-gain antennas. Radio signals were transmitted to and received from the MESSENGER spacecraft at X-band frequencies (7.2-GHz uplink, 8.4-GHz downlink) by the 34-m and 70-m antennas at NASA's Deep Space Network stations in Goldstone, California; Madrid, Spain; and Canberra, Australia.

Mass was also conserved by limiting the number of spacecraft components that moved. With the lone exception of the imaging system (see next section), all science instruments were hard-mounted to the spacecraft. As a consequence, spacecraft attitude often had to be changed continuously in orbit about Mercury to permit the instruments to make their observations.

Spacecraft power was provided by two solar arrays (Figures 1.2 and 1.3), which could be articulated to manage array temperature, and by a battery during those orbits when the spacecraft was on Mercury's nightside and the Sun was eclipsed. In a fully redundant electronics system, a main processor performed all nominal spacecraft functions, while two other processors monitored spacecraft health and safety. The spacecraft attitude control system was three-axis stable and momentum biased and made use of four reaction wheels. Attitude knowledge was acquired through an inertial measurement unit, two star trackers, and a suite of Sun sensors as a backup to the primary attitude sensors.

Primarily passive thermal management techniques were used to minimize heating of spacecraft subsystems by the Sun and the dayside surface of Mercury. To protect the spacecraft from solar heating, all systems except the solar arrays were kept behind a ceramic-cloth sunshade that pointed toward the Sun. This approach simplified the design of the subsystems, which could be built with conventional electronics, but added a substantial constraint to the operation of the spacecraft. Throughout its time within the inner solar system and in orbit about Mercury, MESSENGER was constrained to maintain the orientation of the normal to the central sunshade panel in the sunward direction to within ±10° in Sun-relative elevation angle (pitch) and ±12° in Sun-relative azimuth (yaw) at all times.

1.2.4 Instrument Payload

The project requirements for MESSENGER's primary mission were met by a suite of seven scientific instruments plus the spacecraft communication system (Gold et al., 2001). There was a dual imaging system for wide and narrow fields of view, monochrome and color imaging, and stereo; gamma-ray, neutron, and X-ray spectrometers for surface chemical mapping; a magnetometer; a laser altimeter; a combined ultraviolet–visible and visible–near-infrared spectrometer to survey both exospheric species and surface mineralogy; and a combined energetic particle and plasma spectrometer to

Figure 1.3. View of the MESSENGER spacecraft during vibration testing at the Johns Hopkins University Applied Physics Laboratory. The solar arrays (mirrored surfaces) are stowed in their positions at the time of launch. Also visible are the Magnetometer boom (center), similarly in its stowed position, and thermal blankets (gold).

sample charged species in the magnetosphere (Figure 1.4). Brief descriptions of the payload instruments are as follows.

1.2.4.1 Mercury Dual Imaging System

The Mercury Dual Imaging System (MDIS) on the MESSENGER spacecraft (Hawkins et al., 2007), shown in Figure 1.4, consisted of a monochrome narrow-angle camera (NAC) and a multispectral wide-angle camera (WAC). The NAC was an off-axis reflector with a 1.5° field of view (FOV) and was co-aligned with the WAC, a four-element refractor with a 10.5° FOV and a 12-color filter wheel. The focal-plane electronics of each camera were identical and used a 1024 × 1024 charge-coupled-device detector. Only one camera operated at a time, a design that allowed them to share a common set of control electronics. The NAC and the WAC were mounted on a pivoting platform that provided a 90° field of regard, from 40° sunward to 50° anti-sunward from the spacecraft *z*-axis (Figure 1.2) – the boresight direction of most of MESSENGER's instruments. Onboard data compression provided capabilities for pixel binning, remapping of 12-bit data to 8 bits, and lossless or lossy compression. During MESSENGER's primary mission, four main MDIS data sets were planned: a monochrome global image mosaic at near-zero emission angles and moderate incidence angles, a stereo complement map at off-nadir geometry and near-identical lighting, multicolor images at low incidence angles, and targeted high-resolution images of key surface features. It was further planned that those data would be used to construct a global image base map, a digital terrain model, global maps of color properties, and mosaics of high-resolution image strips.

1.2.4.2 Gamma-Ray and Neutron Spectrometer

The Gamma-Ray and Neutron Spectrometer (GRNS) instrument (Figure 1.4) included separate Gamma-Ray Spectrometer (GRS) and Neutron Spectrometer (NS) sensors (Goldsten et al., 2007). The GRS detector was a mechanically cooled crystal of germanium, and the sensor detected gamma-ray emissions in the energy range 0.1–10 MeV and achieved an energy resolution of 3.5 keV full width at half maximum for ^{60}Co (1332 keV). Special construction techniques provided the necessary thermal isolation to

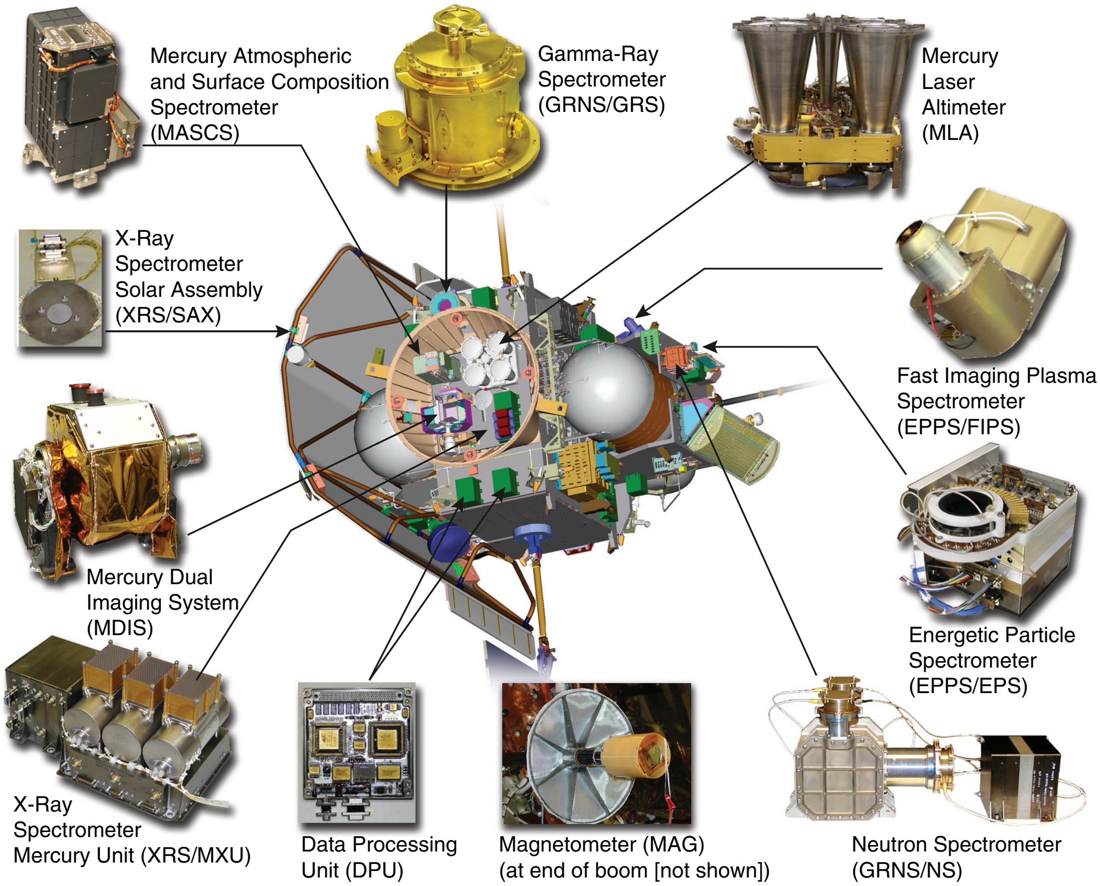

Figure 1.4. MESSENGER instruments and their locations on the spacecraft.

maintain the encapsulated detector at cryogenic temperatures (90 K) despite the high temperatures in Mercury's environment. The outer housing of the GRS sensor was equipped with an anticoincidence shield (ACS) to reduce the background from charged particles. The NS sensor consisted of a sandwich of three scintillation detectors working in concert to measure the flux of neutrons in three energy ranges from thermal to ~7 MeV.

1.2.4.3 X-Ray Spectrometer

The X-Ray Spectrometer (XRS) (Figure 1.4) measured the characteristic X-ray emissions induced on the surface of Mercury by the incident solar X-ray flux (Schlemm et al., 2007). The instrument detected the Kα lines for the elements Mg, Al, Si, S, Ca, Ti, Cr, Mn, and Fe. The planet-viewing sensor (Mercury X-ray Unit, MXU) consisted of three gas-filled proportional counters, one with a thin Mg foil over the entrance window, one with a thin Al foil over the entrance window, and one with no foil to separate the lower-energy lines from Mg, Al, and Si. The 12° field of view of the planet-viewing sensor allowed a spatial resolution that ranged from 42 km at 200-km altitude to 3200 km at 15,000-km altitude. A small Si-PIN detector (Solar Assembly for X-rays, SAX) mounted on the spacecraft sunshade (Leary et al., 2007) and directed sunward provided simultaneous measurement of the solar X-ray flux. The solar detector included a thermoelectric cooler that could also operate in a heater mode to anneal the sensor after radiation damage.

1.2.4.4 Magnetometer

MESSENGER's Magnetometer (MAG) was a low-noise, triaxial fluxgate instrument (Anderson et al., 2007). Its sensor was mounted on a 3.6-m-long boom that was directed generally anti-sunward (Figures 1.2 and 1.3). The instrument had both a coarse range, ±51,300 nT full scale (1.6-nT resolution), for preflight testing, and a fine range, ±1530 nT full scale (0.047-nT resolution), for operation near Mercury. A magnetic cleanliness program followed during the design and construction of the spacecraft minimized variable and static spacecraft-generated fields at the sensor. Analog signals from the three instrument axes were low-pass filtered (10-Hz cutoff) and sampled simultaneously by three 20-bit analog-to-digital converters every 50 ms. To accommodate variable telemetry rates, MAG provided 11 output rates from 0.01 s^{-1} to 20 s^{-1}. The instrument also provided continuous measurement of fluctuations by means of a digital 1–10-Hz bandpass filter. This fluctuation level was used to trigger high-time-resolution sampling in 8-min segments to record events of interest when continuous high-rate sampling was not possible.

1.2.4.5 Mercury Laser Altimeter

The Mercury Laser Altimeter (MLA) (Cavanaugh et al., 2007) (Figure 1.4) measured the round-trip time of flight of transmitted laser pulses reflected from the surface of Mercury which, in combination with the spacecraft orbit position and pointing data, gave a high-precision measurement of surface topography referenced to Mercury's center of mass. The laser transmitter was a diode-pumped Nd:YAG slab laser with passive Q-switching. The transmitter emitted 5-ns-wide pulses at an 8-Hz rate with 20 mJ of energy at a near-infrared wavelength of 1064 nm. The receiver consisted of four refractive telescopes and four equal-length optical fibers to couple the received optical signal onto a single silicon avalanche photodiode. The timing of laser pulses was measured with a set of time-to-digital converters and counters and a crystal oscillator operating at a frequency that was monitored regularly from Earth. MLA sampled the planet's surface to within a 1-m range error when the line-of-sight range to Mercury was less than 1500 km under spacecraft nadir pointing or the slant range was less than ~1000 km at off-nadir angles up to ~40°.

1.2.4.6 Mercury Atmospheric and Surface Composition Spectrometer

MESSENGER's Mercury Atmospheric and Surface Composition Spectrometer (MASCS) (McClintock and Lankton, 2007) consisted of a small Cassegrain telescope with 257-mm effective focal length and a 50-mm aperture that simultaneously fed an Ultraviolet and Visible Spectrometer (UVVS) and a Visible and Infrared Spectrograph (VIRS) (Figure 1.4). UVVS was a 125-mm-focal-length, scanning grating, Ebert–Fastie monochromator equipped with three photomultiplier tube detectors that covered far-ultraviolet (115–180 nm), middle-ultraviolet (160–320 nm), and visible (250–600 nm) wavelength ranges with an average spectral resolution of 0.6 nm. It was designed to measure profiles with altitude of known exospheric species, to search for previously undetected exospheric species, and to observe Mercury's surface in the far and middle ultraviolet at a spatial scale of 10 km or smaller. VIRS was a fixed concave grating spectrograph with a 210-mm focal length equipped with a beam splitter that simultaneously dispersed the spectrum onto a 512-element silicon visible-wavelength photodiode array (300–1050 nm) and a 256-element indium-gallium-arsenide infrared-wavelength photodiode array (850–1450 nm). The VIRS was designed to map surface reflectance with 5-nm spectral resolution in the wavelength range 300–1450 nm.

1.2.4.7 Energetic Particle and Plasma Spectrometer

The Energetic Particle and Plasma Spectrometer (EPPS) instrument on MESSENGER consisted of two sensors (Andrews et al., 2007), an Energetic Particle Spectrometer (EPS) and a Fast Imaging Plasma Spectrometer (FIPS) (Figure 1.4). The EPS was a hockey-puck-sized energy by time-of-flight spectrometer designed to measure in situ the energy, angular, and compositional distributions of the high-energy components of electrons (>20 keV) and ions (>5 keV/nucleon) near Mercury. The FIPS measured the energy, angular, and compositional distributions of the low-energy components of the ion distributions (<50 eV/charge to 20 keV/charge). The FIPS sensor featured an electrostatic analyzer system with a large (1.4 sr) instantaneous field of view.

1.2.4.8 Radio Science

The MESSENGER telecommunications subsystem was designed primarily to send commands to the spacecraft and to transmit to Earth both science measurements and information on the state of the spacecraft and instruments (Srinivasan et al., 2007). The subsystem doubled as a scientific tool by providing precise measurements of the spacecraft's velocity and range along the line of sight to Earth, information essential for spacecraft navigation and also for deriving Mercury's gravity field.

1.2.5 Orbit Design

The parameters selected for the MESSENGER orbit after the orbit insertion maneuver resulted from a complex trade-off of scientific objectives, spacecraft and instrument thermal design, communications and power constraints, and propellant budget (Santo et al., 2001). The original design for the initial orbit featured a periapsis altitude of 200 km, a periapsis latitude of 60°N, an inclination of 80° to the planet's equatorial plane, and a period of 12 h. The periapsis latitude and altitude, the high eccentricity of the orbit, and the phasing of the initial orbit relative to local time and Mercury true anomaly were all selected as part of the mission thermal design. The 12-h period was chosen to regularize the schedule of mission operations and permitted ample time for data downlink near apoapsis.

Orbit-correction maneuvers (OCMs) were planned for the orbital phase of the primary mission, because the gravitational pull of the Sun would raise periapsis altitude and latitude between successive orbits (McAdams et al., 2007). Such maneuvers were planned in pairs, with the first designed to lower periapsis altitude back to ~200 km and the second to adjust the orbit period after the first correction back to 12 h. The pairs of maneuvers were scheduled approximately one Mercury year apart in order to keep periapsis altitude below 500 km while meeting spacecraft sunshade pointing and science requirements.

1.3 MESSENGER'S SCIENCE DATA ACQUISITION PLANNING AND OPERATIONS

Planning for MESSENGER's scientific observations from orbit about Mercury required a novel approach to the design of payload operations and spacecraft attitude-control commanding. Experience with science planning for the Mercury flybys demonstrated the complex interplay between imaging and competing remote sensing observations, as well as with spacecraft operational constraints on pointing, power management, navigation, and achievable rates of change to spacecraft attitude. Planning for the flybys was conducted with conventional manual approaches to the design of observation and spacecraft command sequences with computational and visualization tools. Months of iterative, labor-intensive work were required to design, simulate, and review each encounter. The complexities of operations from orbit about Mercury, however, called for a marked change in the planning architecture, given that the orbital phase of the primary mission phase would be equivalent to two flybys every Earth day. To effect such a change, the observational requirements, spacecraft capabilities, and operational constraints had to be captured in carefully implemented software, which was then used together with orbit solutions in an automated search for optimal observation opportunities and spacecraft attitude, imaging pivot commanding, and instrument commanding. Those objectives were accomplished with a sophisticated, integrated suite of modules known as SciBox (Anderson et al., 2011b; Choo et al., 2014).

1.3.1 Science Observation Constraints

The observational opportunities at Mercury were highly constrained by MESSENGER's eccentric orbit and Mercury's low spin rate. A solar day on Mercury is approximately 176 Earth days, so during MESSENGER's year-long primary orbital mission there were only two opportunities to observe each longitude at a given solar illumination. In addition, the different science investigations had distinct and competing pointing requirements. For monochrome surface imaging, for instance, a specific range of solar incidence angles is optimal to reveal surface features while not obscuring terrain in shadow, whereas for color imaging near-normal solar incidence angles are best. Imaging plans also had to incorporate a favorable phase angle to minimize forward scattering of sunlight yet maintain surface resolution. Moreover, the choice of MDIS camera, wide-angle or narrow-angle, depended on altitude and viewing geometry as well as the need to balance resolution with the requirement to obtain as complete and overlapping imaging coverage as possible.

MESSENGER's other science investigations imposed still different requirements. Most of the instruments on the spacecraft's main instrument deck (Figure 1.4) had co-aligned fields of view and yielded optimal data for near-nadir viewing directions. In contrast, exospheric observations by the UVVS required turning the spacecraft so that the spacecraft z-axis, i.e., the normal to the instrument deck, pointed off the limb of the planet. The MLA observations yielded the highest signal-to-noise ratio for surfaces in darkness, whereas the XRS observations required that the surface be in daylight so as to be exposed to solar X-rays. The GRS observations were largely insensitive to surface illumination, but the NS observations were optimal for specific orientations of the NS detectors with respect to the spacecraft orbital velocity relative to Mercury. Finally, the EPS instrument yielded the most scientifically fruitful data when the magnetic field direction lay in the plane of the instrument field of view.

1.3.2 Spacecraft and Mission Operations Constraints

Over and above the scientific objectives and instrument observational constraints, ensuring the continued health of the spacecraft and payload demanded attention to spacecraft operations, communications, and navigation considerations. The constraints on spacecraft attitude were strictly enforced to maintain the orientation of the normal to the central sunshade panel in the direction of the Sun to within specified tolerances in the Sun-relative elevation angle and azimuth. Violation of these constraints would trigger autonomous spacecraft protection procedures and abort the science observation sequence, so the planning software imposed these constraints as hard limits on the commanded attitude. Communication passes for command uplink and data downlink and spacecraft angular momentum management were carefully planned and reserved for mission operations. Software tools were developed to allocate spacecraft resources, particularly the solid-state recorder (SSR), to track and predict the onboard data volume against the observation plan to ensure the return to Earth of all collected data. Orbit-adjustment maneuvers and other mission-critical activities were also strictly reserved for mission operations planning and treated as unavailable for science observations that required attitude commanding. Passive science data collection continued through communications operations.

1.3.3 Automated Science Opportunity Analyzer and Scheduler

The MESSENGER SciBox suite of software modules was designed to factor in the payload constraints and priorities for observation geometry and range within the constraints of orbit design and mission operations. The SciBox functional structure is shown schematically in Figure 1.5. Because a pivot about the spacecraft–Sun line was incorporated into the MDIS design, the imaging observations could be planned with this additional degree of freedom not available to the other instruments. This capability motivated an altitude-based hierarchy of science pointing priority, by which different instruments were assigned attitude control for specific ranges of altitude. Attitude control was assigned to MLA for all altitudes less than the ranging limit (~1500 km) to the surface for a nadir point on the planet's nightside. Otherwise, pointing control was assigned to XRS on the dayside if the allowed range of directions of the spacecraft z-axis intercepted the planet. The remaining time in which the planet was within the MDIS field of regard was assigned to MDIS control, and the remainder of the observing time was assigned to exosphere observations by MASCS. The science team also identified prioritized sets of specific targets on the planet for focused observation (e.g., high resolution, additional colors, greater pointing dwell time). These targets were assembled into a target database and were selected if unsubscribed opportunities were present. Each instrument was also assigned an allocation for data volume, and a nominal plan for altitude-dependent data collection was designed for each of the instruments other than MDIS.

This database and the mission design were ingested to derive a draft observation plan and predictions for SSR loading for the entire orbital mission. The spacecraft orbit (in the form of kernels in the NASA Spacecraft, Planet, Instrument, C-matrix, Events – or SPICE – toolkit), times reserved for mission operations, and constraints on spacecraft attitude slew rate and MDIS pivot rotation rate (captured as rules) were used by the Opportunity Analyzer in SciBox to identify all possible imaging opportunities. The MDIS imaging plan was then constructed by the Opportunity Analyzer, which identified all achievable imaging opportunities given the spacecraft attitude as constrained by MLA- and XRS-assigned attitude and the MDIS pivot. These opportunities were next evaluated against the desired properties for imaging and requirements for imaging overlap by the Optimizer module, resulting in the generation of an imaging plan and a spacecraft science attitude

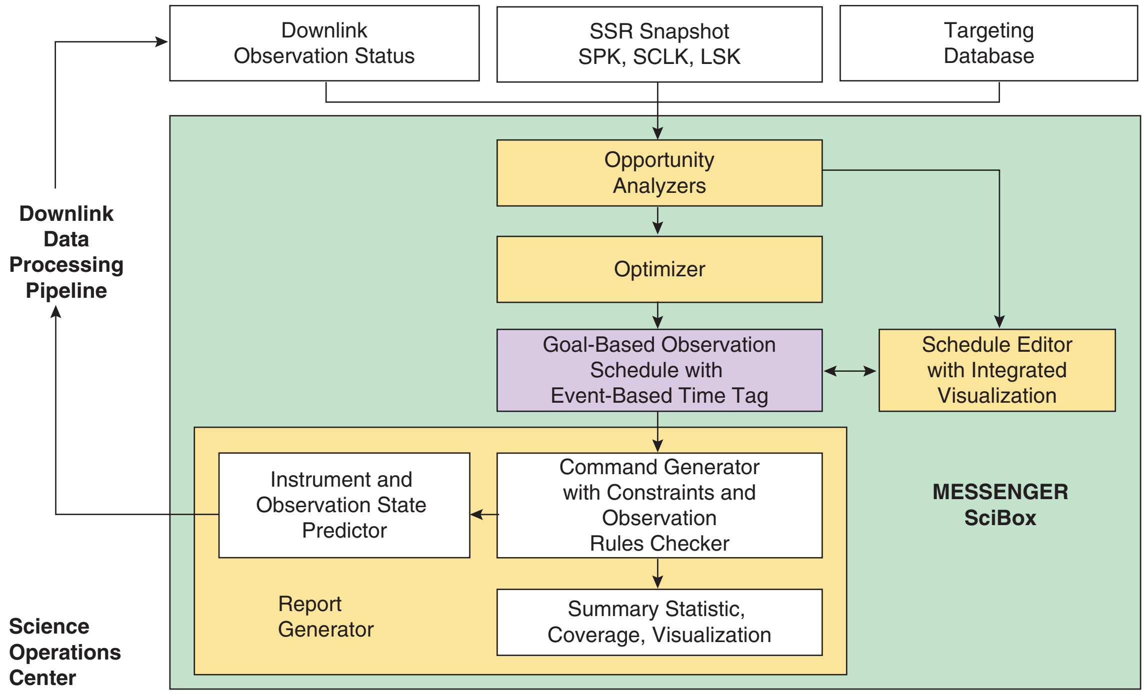

Figure 1.5. Functional schematic of the MESSENGER SciBox software suite (green box). Input data are indicated by white boxes at the top (downlink status, SSR data volume, attitude and orbit data in SPK, SCLK, and LSK SPICE kernels, and the targeting database); the main module elements are indicated by tan boxes; the key intermediate schedule product is indicated by the purple box; and key elements of the report generator are shown. The SciBox software was maintained and configured within the MESSENGER Science Operations Center, and the state predictor was used to update the SSR load predictions. SPK, SCLK, and LSK denote the Spacecraft and Planets Kernel, the Spacecraft Clock Kernel, and the Leapseconds Kernel, respectively.

plan. These plans were then checked against the spacecraft control constraints by the Rules Checker module, and draft spacecraft attitude and instrument commanding sequences were generated. The loading on the SSR was also evaluated and updated, including the expected downlink capacity for each communication pass. One key to ensuring accuracy of the planning against actual performance was that the times of commanding were keyed to orbit events rather than to absolute time. This procedure allowed the plan to transition smoothly from the orbit predictions far in the future to the immediate planned orbit using the latest orbit predictions to generate actual commands for the spacecraft.

The integrated plan was developed with an iterative approach by which successively more observations were included in the Opportunity Analyzer. Once it was demonstrated that the imaging goals could be met within the MLA and XRS constraints, the other pointed observations, including UVVS exosphere and surface targets, were included in the planning. In addition, the predictions for SSR loading were used to tailor the allowed instrument observation rates, and these revised data rates were included in refinements to the mission-long observation plan. Development and refinement of the modules continued throughout the orbital phase, including both extended missions, to track the additional science observation objectives.

1.3.4 Advance and Near-Term Science Planning

The integrated mission plan was used for both science planning and command generation (Berman et al., 2010). The plan was re-derived for each week of operations and updated with information acquired for imaging coverage, SSR loading, and any adjustments needed for instrument performance, operation, or spacecraft operations rules. This analysis constituted the Advance Science Planning process, which was the starting point for building the final command loads for the spacecraft. The command building process, known as Near-Term Science Planning, ran on a four-week cadence. A week's commands were generated four weeks ahead of execution on the spacecraft, and with each successive week the sequence was processed through different stages of review, quality assessment, and error checking. For actual spacecraft commanding, the SciBox suite included converters from the schedules to instrument operation and spacecraft attitude command requests in formats required by the mission operations scheduling and command-load development tools. These command requests were reviewed by the science and engineering teams for each instrument and then processed through the spacecraft command generator to verify compliance with all instrument and spacecraft rules. Each load was then run through the ground spacecraft simulator before being approved for upload and execution on the spacecraft.

1.3.5 Science Observation Performance

The performance of the observation planning during orbital operations resulted in imaging, mapping, and in situ surveys of the planet that met every project requirement for the

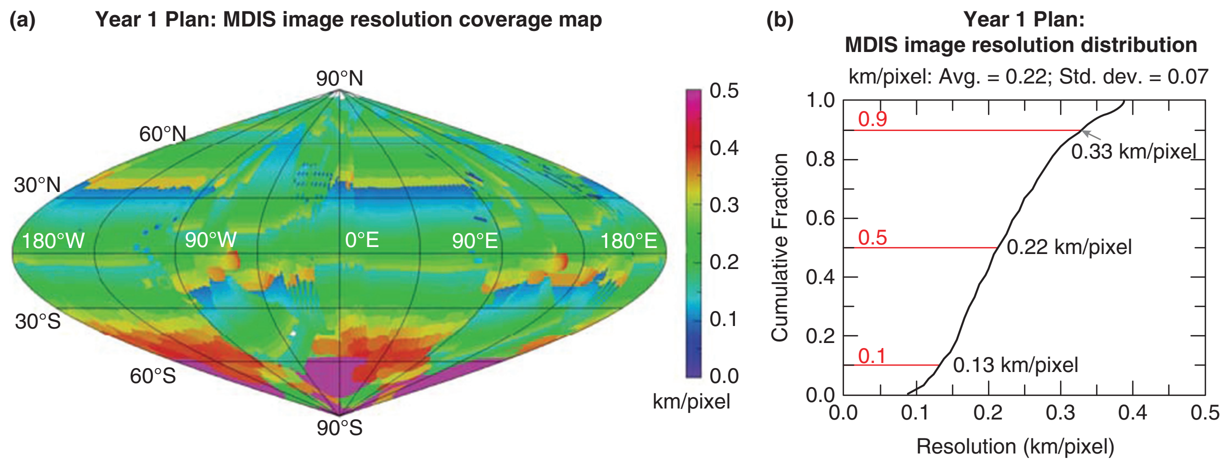

Figure 1.6. Example planning products for the first year of MESSENGER orbital observations, including (a) a map of the MDIS monochrome imaging resolution and (b) the cumulative distribution of image resolution. Products such as these were generated for each instrument to assess the characteristics of the planned observation plan against the observational requirements for each science investigation.

Figure 1.7. Four sequential views of the launch of the MESSENGER spacecraft on 3 August 2004.

mission. This record of mission success hinged critically on the capability of SciBox to design an entire yearlong imaging plan that integrated all of the science observations in a single overarching schedule. As an example, Figure 1.6 shows the planned resolution for MDIS monochrome mapping prior to orbit insertion in the form of a surface map, along with cumulative statistics. Transitions in the resolution over the surface correspond to transitions between the NAC and WAC and merging of imaging obtained on the ascending and descending legs of each orbit. Similar planning maps for image coverage, ensuring overlap to facilitate the construction of mosaics, as well as color imaging, XRS, MLA, VIRS, and GRS coverage, were all generated, and the mission performance met or exceeded all of these plans. Given the complexity of the observation plan and the need to build the entire observation plan at once, it is clear that the automated scheduling tool was essential to the acquisition of the data that allowed all of the advances achieved in our understanding of Mercury's characteristics.

1.4 MESSENGER'S PRIMARY MISSION

1.4.1 Overview of the Primary Mission

MESSENGER launched from Cape Canaveral Air Force Station, Florida, on 3 August 2004 (Figure 1.7). The cruise phase of the mission lasted 6.6 years and included six planetary flybys (McAdams et al., 2005, 2011). A gravity-assist flyby of Earth on 2 August 2005, approximately one year after launch, reduced the spacecraft's perihelion to 0.6 AU and moved the perihelion direction more than 60° closer to that of Mercury. The first of two flybys of Venus on 24 October 2006 increased the inclination of the spacecraft's orbit and reduced the orbit period. The second Venus flyby on 5 June 2007 lowered perihelion sufficiently to permit a Mercury flyby. Both Venus flybys moved the spacecraft's perihelion and aphelion closer to those of Mercury. A single loss of instrument functionality occurred during the primary mission: in April 2005 the high-voltage system on the time-of-flight portion of the EPS sensor failed,

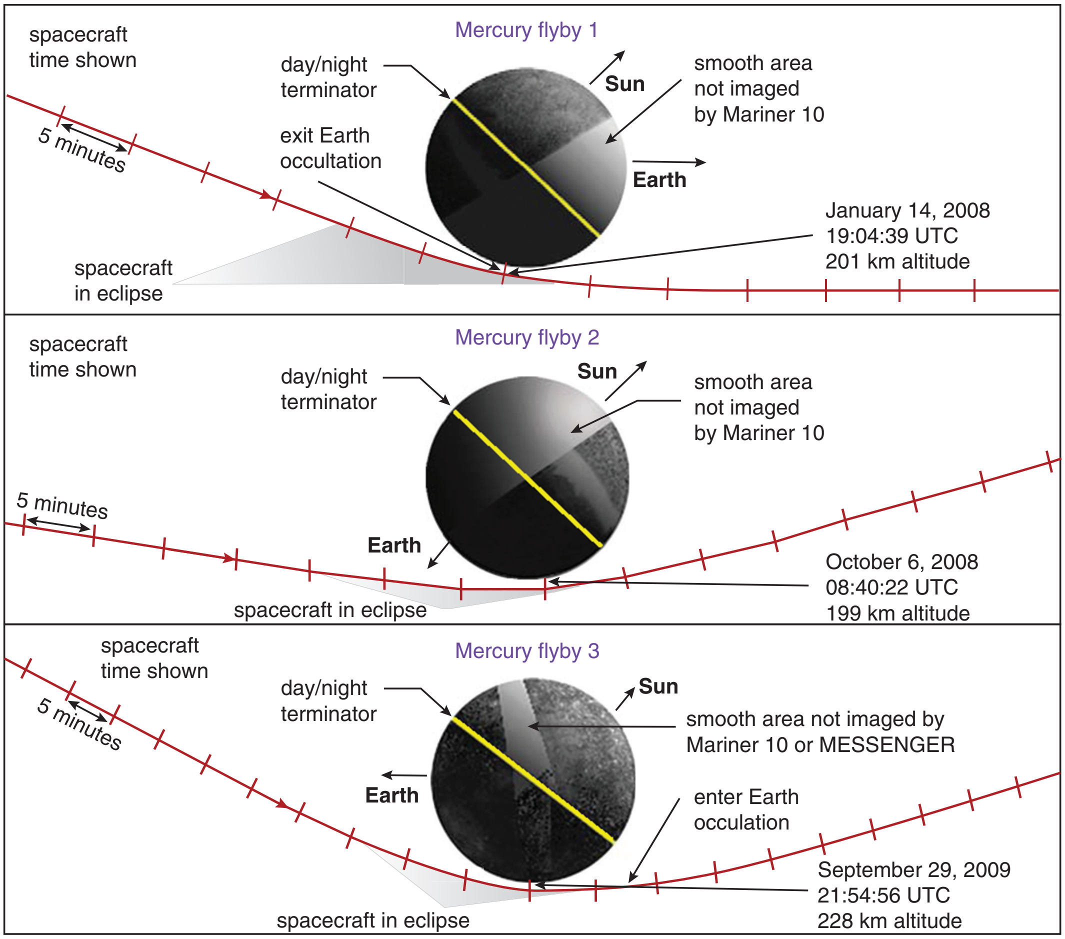

Figure 1.8. MESSENGER's Mercury flyby trajectories as viewed from above Mercury's north pole. Areas not imaged by Mariner 10 are shown in light gray. From McAdams et al. (2011).

and high voltages could not be restored despite repeated attempts over the next several months. The energy subsystem of the sensor (Andrews et al., 2007) was unaffected by this failure and operated until the end of the mission.

MESSENGER executed three flybys of Mercury on 14 January and 6 October 2008 and 29 September 2009. The three flybys, each followed about two months later by a large propulsive course-correction maneuver, completed the rotation of MESSENGER's orbit and changed the period of the orbit progressively closer to that of Mercury (McAdams et al., 2005). Each flyby followed a near-equatorial trajectory and involved closest approach on Mercury's nightside at ~200-km altitude (Figure 1.8). Operationally, the first two flybys proceeded flawlessly, but a safe-hold event triggered by a rising battery temperature shut off data acquisition midway through the third flyby. During the flybys, MESSENGER mapped nearly the entire planet in color, imaged most of the areas unseen by Mariner 10, completed initial measurements of the composition of Mercury's exosphere and neutral tail, and made initial characterizations of the structure and dynamics of Mercury's magnetosphere. Those three flybys returned the first new spacecraft data from Mercury in more than three decades (Figure 1.1). These data were invaluable to the planning of the yearlong orbital phase of MESSENGER's primary mission.

On 18 March 2011, the MESSENGER spacecraft was inserted into a highly eccentric, 12-h orbit about the planet Mercury. The orbit attained had an inclination of 82.5°, an initial periapsis altitude of ~200 km, an initial periapsis longitude of 60°N, and apoapsis at an altitude of ~15,200 km in the southern hemisphere (Figure 1.9).

During the primary mission, the periapsis altitude increased progressively and periapsis latitude drifted northward, both the effect of perturbations to the spacecraft trajectory by the gravitational pull of the Sun. A series of propulsive OCMs was designed to maintain the periapsis altitude within the approximate range 200–500 km (McAdams et al., 2012). OCM-1 and OCM-3 each lowered the periapsis to 200 km, but each maneuver also reduced the orbit period by ~15 min and so was followed by a smaller OCM that returned the period to ~12 h (Figure 1.10). Neither OCM-5 nor OCM-6 was followed by a maneuver to correct the orbit period.

1.4.2 Results from the Primary Mission

By the conclusion of MESSENGER's primary mission, all of the scientific objectives (Table 1.1) had been met, and all of the project requirements (Table 1.2) had been successfully accomplished. Scientific results from MESSENGER's primary mission substantially answered the six questions that had framed the mission.

1.4.2.1 Mercury's High Ratio of Metal to Silicate

Prior to the MESSENGER mission, most hypotheses put forward to explain Mercury's anomalously high core fraction invoked high-temperature processes that would have substantially depleted the planet's inventory of volatile elements. However, elemental measurements of Mercury's surface by MESSENGER's XRS and GRNS instruments during the orbital phase of the primary mission (Nittler et al., 2011; Peplowski et al., 2011; Evans et al., 2012) indicated that such moderately volatile elements as Na, K, and S are not depleted relative to other terrestrial planets. To the contrary, the surface S abundance is at least a factor of 10 higher than that of the surface of Earth or the Moon (Nittler et al., 2011). MESSENGER XRS and GRS measurements during the primary mission also showed that Mercury's surface material is low in iron (no more than ~4 wt% Fe) (Nittler et al., 2011; Evans et al., 2012). Collectively, these results are inconsistent with formation models calling for extended periods of high temperatures (e.g., evaporation in a hot solar nebula, formation from high-temperature condensates, or some giant impact scenarios) and suggest that Mercury's metal-rich, FeO-poor composition likely reflects chemically reduced precursory materials (Nittler et al., 2011), enriched in Fe metal by some aspect of the accretion process.

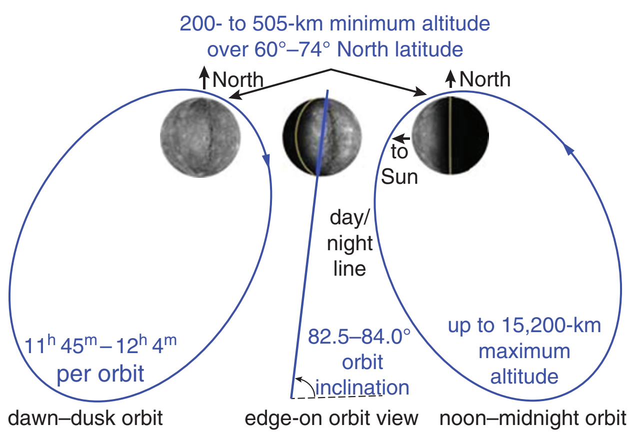

Figure 1.9. Three views of MESSENGER's 12-h orbit during the primary mission: a dawn–dusk orbit viewed from the Sun, an edge-on view, and a noon–midnight orbit viewed from a direction orthogonal to the planet–Sun line. From McAdams et al. (2012).

1.4.2.2 Mercury's Geological History

Global monochrome, color, and stereo images acquired during the Mercury flybys and from orbit revealed the presence of a range of landforms known to be associated with volcanism on other planets, and several lines of evidence suggested that the emplacement of Mercury's surface material has been dominated by volcanism. Indicators of volcanic resurfacing included extensive smooth plains that embay topographic lows, commonly with distinct reflectance and color properties; depressions that may be source vents (Head et al., 2008, 2011); a deficiency of large basins compared with the Moon, probably the result of volcanic burial (Fassett et al., 2012); and broad channels between plains deposits formed by sculpting of surrounding terrain, consistent with large-scale floods of highly fluid material (Byrne et al., 2013; Hurwitz et al., 2013). The similarity of observed features to fluvial landforms is consistent with formation by high-temperature lavas, as also suggested by the Mg-rich nature of Mercury's surface materials (Nittler et al., 2011). Laser altimetry by the MESSENGER spacecraft yielded a topographic model of the northern hemisphere of Mercury (Zuber et al., 2012), showing that the dynamic range of elevations is considerably smaller than those of Mars or the Moon. The most prominent topographic feature was found to be a broad lowland at high northern latitudes which hosts a large volcanic plains deposit covering ~6% of the planet (Head et al., 2011). Explosive volcanism was indicated by ~50 rimless depressions surrounded by diffuse, bright haloes that exhibit redder color

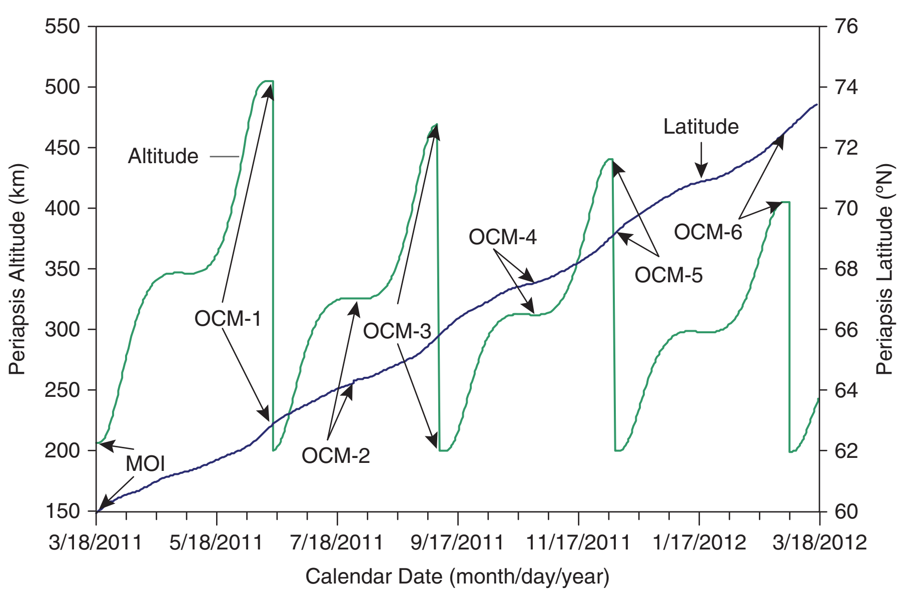

Figure 1.10. Progression of the altitude (green line) and latitude (blue line) of periapsis during MESSENGER's primary mission. The times of Mercury orbit insertion (MOI) and the six orbit-correction maneuvers (OCMs) during the primary mission are shown. From McAdams et al. (2012).

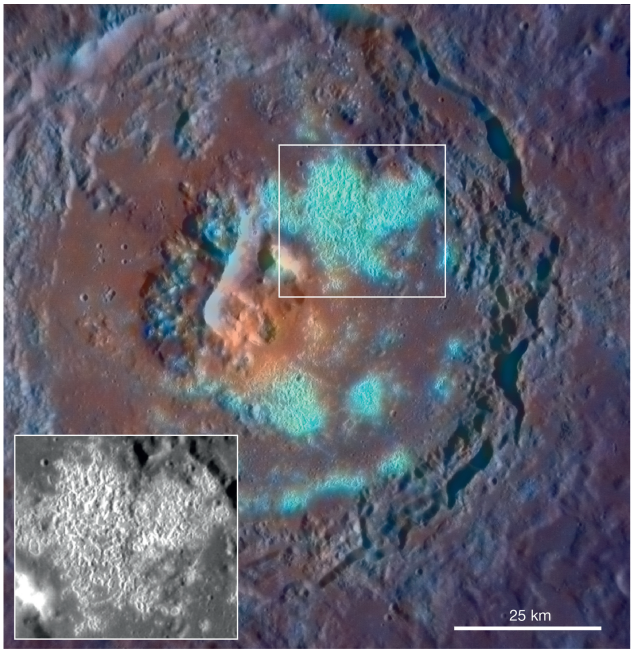

Figure 1.11. Hollows in Tyagaraja crater, 97 km in diameter. Bright areas shown in blue and with etched texture correspond to a high density of hollows (inset). The pit surrounded by reddish material in the center of the crater has been interpreted as a pyroclastic vent. From monochrome image EN0212327089 M, 111 m/pixel, with enhanced color from the eight-filter set EW0217266882I. From Blewett et al. (2011).

than plains materials, and are interpreted as pyroclastic deposits by analogy with such material on the Moon (Kerber et al., 2009; Goudge et al., 2014). Crater size–frequency distributions and stratigraphic analyses suggested that Mercury's smooth plains formation continued into the second half of Mercury's history on local scales, e.g., in the Rachmaninoff basin (Prockter et al., 2010).

One of the most surprising discoveries of the primary mission was the presence of "hollows," fresh-appearing, rimless depressions, commonly with high surface reflectance and often with bright haloes (Figure 1.11). Hollows appear concentrated in the low-reflectance material (LRM) color unit (Robinson et al., 2008; Denevi et al., 2009) within impact craters and basins (Blewett et al., 2011, 2013), and the fact that they are found within some of the freshest craters on Mercury suggests that their formation has been recent or even is ongoing. The host rocks are inferred to have been excavated from depth by impact (Robinson et al., 2008; Denevi et al., 2009), and likely formation mechanisms involve recent loss of volatiles through sublimation, space weathering, pyroclastic volcanism, or outgassing (Blewett et al., 2011, 2013).

1.4.2.3 Mercury's Magnetic Field

Orbital measurements revealed the structure of Mercury's internal magnetic field for the first time. On the basis of crossings of the magnetic equator, the internal field was shown to be consistent with that of a spin-aligned dipole with a moment of 195 ± 10 nT R_M^3; the tilt of the dipole from the spin axis is <0.8° (Anderson et al., 2011a, 2012; Johnson et al., 2012). One of the most surprising results of the MESSENGER mission is that the magnetic dipole is offset from the planet's equator by 479 ± 6 km, or ~0.2 R_M, so that the surface field is larger in magnitude by a factor of ~3 at the north pole than at the south pole, and the surface area of open magnetic flux in the southern hemisphere is larger by a factor of ~4 than in the northern hemisphere. The field geometry points to a core dynamo as the source of the field. Such an axially symmetric yet equatorially asymmetric dynamo is novel for the inner planets, and the low strength of multipolar terms higher than quadrupole is consistent with a deep source for the dynamo (Anderson et al., 2012). Magnetospheric measurements also revealed that Mercury's polar regions are important sources of Mercury's ionized exosphere (Zurbuchen et al., 2011). Further, bursts of energetic electrons were seen at a range of latitudes and times of day, implying that efficient acceleration mechanisms operate within Mercury's magnetosphere on a regular basis and produce electrons with energies up to hundreds of keV on timescales of seconds (Ho et al., 2011).

MESSENGER primary mission observations showed that Mercury's magnetosphere acts more effectively than anticipated to energize solar wind plasma and channel it to the surface. Magnetic reconnection between the planetary and solar wind magnetic fields at Mercury occurs with an intensity an order of magnitude greater than at Earth (Slavin et al., 2012a, b; DiBraccio et al., 2013), and shear instabilities at the magnetopause display similarly greater growth rates (Sundberg et al., 2012a). These interactions yield plasmas within 1000 km of the planetary surface with pressures often exceeding the magnetic pressure (Korth et al., 2011, 2012), leading to intense precipitation to the planetary surface (Winslow et al., 2012). The nearly ubiquitous occurrence of waves driven by ion-plasma instabilities indicates that non-thermal processes are central to plasma dynamics and precipitation behavior (Boardsen et al., 2012). Magnetic reconnection in the tail was also shown to be prevalent and intense, implying that plasmas are energized in the tail and convected convulsively planetward (Slavin et al., 2012a; Sundberg et al., 2012b).

1.4.2.4 Mercury's Core

MESSENGER primary mission data provided considerable insights into Mercury's interior structure. Radio tracking of the MESSENGER spacecraft provided a model of Mercury's gravity field (Smith et al., 2012); when combined with Earth-based measurements of Mercury's spin properties (Margot et al., 2012), the second-harmonic-degree coefficients in the gravity field yielded moments of inertia consistent with a core of ~2020-km radius (Hauck et al., 2013). The silicate mantle and crust together are no more than ~420 km thick, and in the northern hemisphere several large gravity anomalies, including candidate mass concentrations (mascons), exceed 100 mGal in amplitude (Smith et al., 2012; Hauck et al., 2013). From a model of a crust uniformly less dense than the mantle and laterally variable in thickness that fits the northern hemisphere topography and gravity field, Mercury's crust is thicker (50–80 km) at low northern latitudes and thinner (20–40 km) in the north polar region, and shows evidence for thinning beneath some impact basins such as Caloris (Zuber et al., 2012). A model for Mercury's radial density distribution consistent with these results includes a solid silicate crust and mantle overlying a liquid iron-rich outer core, with an overlying solid layer of iron sulfide and a solid inner core possible but not required (Smith et al., 2012; Hauck et al., 2013).

1.4.2.5 Mercury's Polar Deposits

Repeated imaging of Mercury's poles during MESSENGER's primary mission allowed the characterization of craters hosting radar-bright polar deposits, first identified two decades earlier from ground-based radar observations and postulated to consist of water ice (Slade et al., 1992; Harmon and Slade, 1992; Harmon et al., 2011). Mapping the areas of permanent and persistent shadow near each pole showed that nearly all such steadily shadowed regions at the highest latitudes host radar-bright material (Chabot et al., 2012, 2013). Small craters were shown to exhibit radar-bright material, as were craters that extend to latitudes equatorward of ±70°N. Thermal models that incorporate reflected sunlight and infrared radiation from the walls of idealized bowl-shaped craters (Vasavada et al., 1999) are inconsistent with the geologically long-term preservation of near-surface water ice in these small craters, supporting the inference that at least some of the polar deposits are geologically recent.

Neutron Spectrometer data collected during MESSENGER's primary mission indicated that Mercury's radar-bright polar deposits contain, on average, a hydrogen-rich layer more than tens of centimeters thick, generally covered by a surficial layer 10–30 cm thick that is less rich in hydrogen (Lawrence et al., 2013). Active measurements by the MLA of near-infrared (1064-nm wavelength) surface reflectance in permanently shadowed areas near Mercury's north pole revealed regions markedly darker and brighter than Mercury's average surface (Neumann et al., 2013). Both the MLA-dark and MLA-bright regions were shown to be collocated with areas of high radar backscatter in regions of persistent shadow. Correlation of observed reflectance with modeled surface and near-surface temperatures (Paige et al., 2013) indicated that the optically bright regions are consistent with the presence of surficial water ice, whereas MLA-dark regions have temperature structures consistent with water ice buried beneath an insulating surface layer of another volatile material, most likely complex organic deposits stable to somewhat higher temperatures than water ice. Impacts onto Mercury of comets or volatile-rich asteroids could have provided both the water ice and the dark, organic-rich material.

1.4.2.6 Mercury's Volatiles

As mentioned above, orbital data from MESSENGER's primary mission showed higher than expected surface abundances of volatile elements at the surface, including Na, K, and S. Correlation between Ca and S abundances (Nittler et al., 2011) suggested that at least some of the surface S is hosted by calcium sulfides. It was recognized by the end of the primary mission that volatile-rich materials, possibly including sulfides, play important roles in the formation of hollows (Blewett et al., 2011, 2013) and may have helped to drive the explosive volcanic eruptions that emplaced pyroclastic deposits (Kerber et al., 2009; Goudge et al., 2014).

Primary mission observations showed that Na, Ca, and Mg are the dominant species in Mercury's exosphere. Sodium is generally the most abundant and exhibits a two-component structure indicative of multiple source processes that supply Na with different energies (Killen et al., 2012). Calcium and Mg were seen to be less abundant overall and to show predominantly single-component altitude profiles reflective of a high-energy process. All three species show distinct variations in dayside near-surface densities: the Na abundance was seen to peak at local noon, whereas Ca showed a decreasing dawn-to-dusk gradient, and Mg was observed to be nearly isotropic (Burger et al., 2012; Merkel et al., 2012). The distinct distributions among these three species indicated that they are controlled by different source and transport mechanisms. Surveys conducted for other species yielded mostly upper limits. A weak O emission was detected above the subsolar point, and H, likely originating primarily from solar wind implantation, was routinely observed on the dayside and showed an altitude behavior similar to that observed during the Mariner 10 and MESSENGER flybys (Vervack et al., 2011).

1.5 MESSENGER'S FIRST EXTENDED MISSION

After MESSENGER successfully completed its primary mission on 18 March 2012, all spacecraft subsystems and payload instruments were healthy and sufficient propellant remained to continue orbital operations for at least an additional Earth year. Because a second Earth year of observations would provide a substantial advance in our understanding of Mercury beyond what was achieved as of the end of the primary mission, the MESSENGER team had earlier proposed and NASA had approved a first extended mission that lasted one Earth year, i.e., until 18 March 2013.

There were several overarching themes for MESSENGER's first extended mission which ensured that the second year of orbital operations would not be a simple continuation of the primary mission, including operation during a more active Sun, greater focus on observations at low spacecraft altitudes, and a greater variety of targeted observations. The extended mission permitted the first close-in observations of Mercury near a maximum in the solar cycle. A lower average altitude would be accomplished by reducing the period of the spacecraft orbit. The greater variety of targeted observations was enabled by the successful accomplishment of the global mapping objectives of the primary mission.

1.5.1 Objectives for the First Extended Mission

Six science questions framed the first extended mission. Each was motivated by discoveries made during the primary mission,

Table 1.3. *Scientific objectives for MESSENGER's first extended mission.*

1. Determine the morphological and compositional context of hollows and their relation to bright crater-floor deposits and pyroclastic vents.
2. Acquire targeted, high-resolution observations of volcanic materials of low impact crater density identified in the primary mission.
3. Document changes in long-wavelength topography versus geological time on Mercury from altimetric and complementary imaging measurements.
4. Characterize regions of enhanced exospheric density versus solar distance, proximity to geologic units, solar activity, and magnetospheric conditions.
5. Measure changes in exospheric neutrals and plasma ions as solar activity increases.
6. Infer sources and energization mechanism from the location, energy spectra, and temporal profiles of energetic electrons.

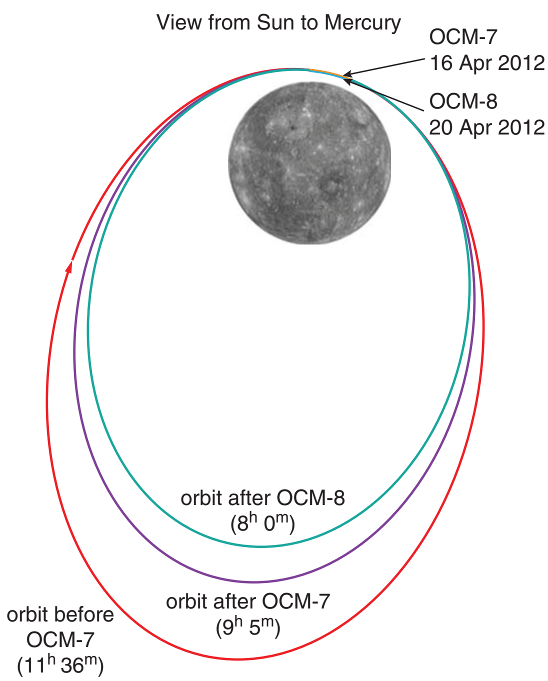

Figure 1.12. Orbit-correction maneuvers OCM-7 and OCM-8 in April 2012 changed MESSENGER's orbit period from just under 12 h to 8 h. North is up. From McAdams et al. (2012).

and collectively they addressed a broad range of coupled issues regarding Mercury's interior, surface, exosphere, and magnetosphere. Those six questions were as follows:

(1) What are the sources of surface volatiles on Mercury?
(2) How late into Mercury's history did volcanism persist?
(3) How did Mercury's long-wavelength topography change with time?
(4) What is the origin of localized regions of enhanced exospheric density at Mercury?

Table 1.4. *Project requirements for MESSENGER's first extended mission.*

1a. Image 70% of the planet in three colors at 600-m/pixel average spatial resolution.
1b. Acquire 100 sets of targeted images of hollows or pyroclastic vents at 60-m/pixel average spatial resolution.
1c. Acquire 20 targeted VIRS observations of hollows and pyroclastic vents at low solar incidence angle (i).
2. Acquire 30 sets of targeted images of young volcanic materials at 60-m/pixel average spatial resolution.
3a. Image 70% of the planet at 250-m/pixel average spatial resolution, targeting i ~ 40°–65°.
3b. Image 70% of the planet at 250-m/pixel average spatial resolution, targeting i ~ 75°–85°.
3c. Provide topographic profiles over 10 broadly elevated regions and the floors of 50 complex impact craters, including volcanically flooded craters.
4a. Survey dayside and nightside exosphere emissions at an average rate of once every third orbit.
4b. During dawn–dusk seasons, conduct repeated observations of exospheric emission over both poles to the maximum extent permitted by spacecraft pointing constraints.
4c. Conduct full-orbit, exosphere observation campaigns at equally spaced Mercury true anomalies over each of four Mercury years.
5. Measure the global distribution of planetary ions and the direction of plasma flow, within operational constraints.
6. Provide locations, energy spectra and pitch angles, and temporal profiles of energetic electrons across all magnetic longitudes in the northern hemisphere.

(5) How does the solar cycle affect Mercury's exosphere and volatile transport?
(6) What is the origin of Mercury's energetic electrons?

Those questions led to the set of scientific objectives for MESSENGER's first extended mission listed in Table 1.3. The project requirements corresponding to those objectives are listed in Table 1.4.

1.5.2 Results from the First Extended Mission

Less than five weeks after the start of the first extended mission, two OCMs four days apart in April 2012 reduced the period of MESSENGER's orbit from just under 12 h to 8 h (Figure 1.12). In its new orbit, the spacecraft spent more time per Earth day near Mercury's surface than during the primary mission. The periapsis altitude was ~280 km at the time of the two OCMs, which reduced the apoapsis altitude to ~10,300 km. Through most of the first extended mission, which saw no further OCMs, the periapsis altitude continued to increase progressively, and the periapsis latitude continued to drift northward. In early March 2013, when the periapsis altitude was ~450 km and the periapsis latitude was ~84°N, the changes to each quantity with successive orbits reversed sign, so that the periapsis moved progressively southward and downward thereafter.

All of the science objectives and project requirements for the first extended mission were achieved by the end of the second year of orbital operations, and substantial progress was made on the six science questions that provided the rationale for the mission extension.

1.5.2.1 Sources of Surface Volatiles

Targeted imaging of hollows during the first extended mission showed that well-developed hollows display a locally constant base level, suggesting either ablation of a layer having locally constant thickness or the development of a thermally insulating and mechanically resistant lag deposit that resists further volatile loss after reaching a given thickness (Blewett et al., 2013). The high abundance of S in Mercury's crust (Nittler et al., 2011; Weider et al., 2012), the instability of some sulfides at low pressure at Mercury's surface temperature (Helbert et al., 2013), and the concentration of hollows on sunward-facing slopes (Blewett et al., 2013) lent support to the hypothesis that hollows form by the ablation of sulfide-rich material within LRM deposits at Mercury's high daytime temperatures (Blewett et al., 2013). Analysis of orbital GRS observations yielded measurements of the surface abundance of Cl and indicated a chondritic Cl/K ratio and a higher abundance at high northern latitudes than nearer the equator, consistent with a role for Cl as a magmatic volatile in the eruption of the northern smooth plains (Evans et al., 2015).

1.5.2.2 History of Volcanism on Mercury

During MESSENGER's first extended mission, more detailed investigations were made of the composition and stratigraphy of Mercury's volcanic units, providing information about the volcanic contributions to the crust over time. XRS and GRS data showed that the northern smooth plains and Caloris interior plains have lower contents of Mg, Ca, and S and higher contents of Al and K (Weider et al., 2012; Peplowski et al., 2012) than do older intercrater plains and heavily cratered terrain, although K at low latitudes and near Mercury's hot poles may be continually removed by heating and redeposited at high latitudes (Peplowski et al., 2012). Only with the added observation time provided by the first extended mission did the coverage of high-energy XRS spectra reach the point at which regional variations in composition could begin to be mapped for other portions of the planet, in particular variations in Fe (Weider et al., 2014). Cratered and intercrater plains that predated the Caloris basin show some evidence for volcanic emplacement and may be older versions of the smooth plains (Denevi et al., 2009, 2013; Whitten et al., 2014). Low lava viscosities implied by flow features within the northern smooth plains are consistent with a composition intermediate between basaltic and ultramafic materials (Byrne et al., 2013; Hurwitz et al., 2013), as suggested by elemental abundance data.

Imaging during the primary and first extended MESSENGER mission revealed new details on the interplay between volcanism and tectonics on Mercury. Deformation within Mercury's large impact basins has been particularly complex and characterized by a diverse range of extensional and contractional features. The two largest basins, Rembrandt (Watters et al., 2009a) and Caloris (Byrne et al., 2012; Klimczak et al., 2013), each display complicated patterns of radial and concentric ridges and troughs, the age relations of which differ between the basins. Mechanisms that may have contributed to intrabasin deformation include loading of the basin interior by volcanic plains deposits and uplift of the basin floor by some combination of exterior loading and inward subsurface flow. Extensional deformation also occurred in buried, lava-filled basins and craters (Klimczak et al., 2012; Watters et al., 2012), probably as a result of cooling of the surficial lavas (Freed et al., 2012), and on at least one plateau, possibly a product of the relaxation of topographic relief.

1.5.2.3 Changes in Mercury's Long-Wavelength Topography

Global image mosaics of Mercury with lighting favorable to the characterization of morphology and stereo coverage plus MLA altimetry revealed a picture of Mercury's global tectonics far more complicated than the view immediately following the MESSENGER flybys, which emphasized lobate scarps and high-relief ridges as accommodators of global contraction (Watters et al., 2009b). Topography on Mercury is dominated not by impact basins, as on the Moon and Mars, but by broad rises (Preusker et al., 2011; Zuber et al., 2012). Some of these rises are superimposed on earlier volcanic flow features, occur within the otherwise low-relief northern smooth plains, and bow the floor of Caloris basin to elevations above the rim (Klimczak et al., 2013). On the northern smooth plains, outwardly tilting floors of volcanically infilled craters on the broad northern rise suggest that long-wavelength deformation postdated volcanism, and similar relations are seen on the long-wavelength topographic rises in Caloris and elsewhere (Balcerski et al., 2013). Some sets of lobate scarps bound broad rises that form monoclinal or anticlinal plateaus; such scarp systems are hypothesized to be outward-verging thrust faults in deformational assemblages that display similarities to terrestrial fold-and-thrust belts (Byrne et al., 2014).

1.5.2.4 Regions of Enhanced Exospheric Density

The evidence acquired during the primary mission for localized regions of enhanced exospheric density led to targeted observations during the first extended mission aimed at mapping their occurrence and understanding their origin. These observations revealed an exosphere in which the three most easily detected species – Na, Ca, and Mg – behave in ways not only different from one another but also at odds with hypotheses put forward to account for ground-based observations. The strong Ca enhancement in the dawn equatorial region, discovered during the MESSENGER flybys, showed persistence in both location and abundance (Burger et al., 2014) yet was seen to be composed of atoms too energetic to be derived from a strictly solar-release process, as the dawn location might suggest (Burger et al., 2012). An enhancement in Mg was seen near dawn local times, a phenomenon particularly notable near perihelion (Merkel et al., 2012, 2017).

In contrast to Ca and Mg, the Na exosphere exhibited less-marked localized enhancements, showing at most limited dawn–dusk asymmetry, contrary to many observations from the ground (Cassidy et al., 2015). Most surprising in the Na exosphere, however, was the general lack of short-term spatial and temporal variability in the MESSENGER observations, a result at odds with that seen in ground-based data (Killen et al., 2012). Whereas the Ca asymmetry would have been missed in ground-based observations owing to the limited geometry afforded from Earth, short-term variations in Na should not be as susceptible to differences in large-scale geometry. Instead, this difference between MESSENGER and ground-based observations suggests that the short-term variations originate almost completely in mid- to high-latitude dayside regions of the exosphere poorly probed by MESSENGER.

1.5.2.5 Effect of the Solar Cycle on Mercury's Neutral and Ionized Exosphere

Campaign observations spaced regularly through Mercury's orbit during the first extended mission, combined with daily measurements of the dayside and nightside exosphere during both the primary and first extended missions, revealed the overall behavior of the Na, Ca, and Mg exospheres over several Mercury years. All three species exhibited a relative persistence from year to year in the overall exospheric morphology, with seasonal variations in emission intensity in general agreement with that expected from variations in solar flux with Mercury true anomaly (Merkel et al., 2012, 2017; Burger et al., 2014; Cassidy et al., 2015). Contemporary magnetospheric measurements revealed a highly time-variable and spatially structured particle environment. Enhancements in planetary plasma ions were found in the dawn equatorial region, similar to neutral Ca enhancements, whereas on the nightside, observed asymmetries in planetary ions may be evidence of non-adiabatic behavior, expected but not previously observed (Raines et al., 2013). Despite the presence of localized enhancements in both the exosphere and magnetosphere, which suggest that feedback among these two systems and the surface is highly complex, the large-scale structure of the exosphere showed surprisingly little variation with changing solar conditions during the first two years of orbital observations. This finding was contrary to the expectations from current understanding of sputtering and other surface-interaction processes and the observed highly dynamic nature of the magnetosphere.

1.5.2.6 Mercury's Energetic Electrons

The existence of bursts of energetic electrons in Mercury's magnetosphere, a major discovery during the Mariner 10 flybys, was suggested by XRS signals seen during MESSENGER's Mercury flybys (Slavin et al., 2008) and confirmed almost as soon as MESSENGER began orbital science observations (Ho et al., 2011). Measurements during MESSENGER's primary and first extended mission revealed two groups of energetic electron events, one concentrated at northern high latitudes on the nightside and the other near the geographic equator at most local times (Ho et al., 2012). Not only were the two groups found at different spatial locations, but they also differed in energy distribution, with the high-latitude group tending to have energies in excess of 35 keV and the equatorial population having lower energies in the range 1–10 keV. Frequent observations of X-rays from Mercury's nightside surface, interpreted as X-ray emission induced by the interaction with ~1–10-keV electrons, indicated that the energetic electrons seen in orbit often precipitated onto Mercury's surface (Starr et al., 2012). Most of the observed energetic electron events displayed similar profiles of intensity versus time, with increases above background by up to three orders of magnitude within a few seconds (Ho et al., 2012). Although the spatial and large-scale temporal occurrence of these events was mapped, the unexpectedly irregular nature of these events, with the rapid rise in intensity and a velocity dispersion on timescales too short to be resolved by the EPS, hindered attempts to pin down the source or the acceleration mechanism. During the first extended mission, in June 2012, the cryocooler for the GRS sensor ceased to function at a time closely corresponding to its anticipated end of life. The ACS on the GRS nonetheless remained operational, and near the end of the first extended mission in February 2013 it was repurposed to measure energetic particles at a 10-ms sampling rate.

1.6 MESSENGER'S SECOND EXTENDED MISSION

MESSENGER's first extended mission raised new questions about Mercury that could be addressed only with new measurement campaigns. Given the healthy state of the spacecraft and instrument payload, an ample power margin, and remaining propellant as the end of the first extended mission drew near, the MESSENGER team proposed to NASA and the agency approved a second extended mission approximately two Earth years in duration. The questions that framed the second extended mission followed from discoveries made earlier in the mission or anticipated special aspects of either the timing of the observations or the geometry of MESSENGER's orbit. These questions addressed processes that have recently affected Mercury's surface, particularly at the locations of Mercury's hollows; the evolution of stress in Mercury's crust, and how that stress has been accommodated by a remarkably diverse set of tectonic landforms; changes in the composition of volcanic materials through geological time, and their implication for the evolution of magmatic source regions; the characteristics of volatile emplacement and sequestration in areas of permanent shadow in Mercury's north polar region; the consequences to Mercury's surface and neutral and ionized exosphere of the surface impact of ions and energetic electrons; the response of Mercury's exosphere and magnetosphere to continuing changes in solar activity; and the evolution of Mercury's crust and deeper interior as revealed by observations sensitive to variations over short horizontal scales.

A critical aspect of MESSENGER's second extended mission from the perspective of Mercury's exosphere, magnetosphere, and heliospheric environment was that the maximum in the solar cycle during which the mission had operated was predicted to occur during the first year of second extended mission operations, and the remainder of that year and all of the second year would capture the waning phase of the solar cycle. Solar disturbances were predicted to transition from coronal mass ejections (CMEs) up to and through solar maximum to high-speed streams during the declining phase of the cycle. It was recognized that the second extended mission therefore afforded a distinctive opportunity to characterize the response of Mercury's magnetosphere and exosphere to highly contrasting and intense forcing qualitatively different from that observed to date.

The second year of MESSENGER's second extended mission would also feature periapsis altitudes lower than at any earlier time in the mission, i.e., closer to Mercury's surface than any spacecraft had been before. Through the natural evolution of MESSENGER's orbit in response to the gravitational attraction of the Sun, together with an optimized set of OCMs conducted with MESSENGER's remaining propellant, it was planned that the spacecraft orbit during the final year would feature four separate campaigns of several days to one week each, during which the periapsis altitude would be nearly steady at 25 to 15 km. Such campaigns would provide opportunities to observe regions of Mercury at resolutions markedly superior to those yet attained, across the full suite of instruments. Observations would continue to extraordinarily low altitudes until the spacecraft finally impacted the planet at the end of mission operations.

1.6.1 Objectives for the Second Extended Mission

Seven science questions framed the second extended mission. Each was motivated by discoveries made during the primary and first extended missions, and collectively they addressed broad aspects of Mercury's characteristics, history, and interaction with the inner heliosphere. Those seven questions were as follows:

(1) What active and recent processes have affected Mercury's surface?
(2) How has the state of stress in Mercury's crust evolved over time?
(3) How have the compositions of volcanic materials on Mercury evolved over time?
(4) What are the characteristics of volatile emplacement and sequestration in Mercury's north polar region?
(5) What are the consequences of precipitating ions and energetic electrons at Mercury?
(6) How do Mercury's exosphere and magnetosphere respond to both extreme and stable solar wind conditions during solar maximum and the declining phase of the solar cycle?
(7) What novel insights into Mercury's thermal and crustal evolution can be obtained with high-resolution measurements from low altitudes?

Those questions led to the set of scientific objectives for MESSENGER's second extended mission listed in Table 1.5; the first number of each objective is tied to the corresponding science question. That the list of scientific objectives was longer than for the primary or first extended mission was a reflection of the maturation of our knowledge of the planet during the mission and the breadth and diversity of issues raised by the first two years of orbital observations. The project requirements corresponding to those objectives are listed in Table 1.6; many of the project requirements satisfied multiple science objectives.

1.6.2 Results from the Second Extended Mission

The design of the second extended mission combined optimum use of remaining propellant with spacecraft pointing strategies that balanced episodes of more intense heating of the spacecraft with opportunities for observations at lower altitudes than earlier in the mission (McAdams et al., 2014). The evolution of the altitude and latitude of periapsis during all but the final few weeks of the extended mission is illustrated in Figure 1.13. No OCMs were conducted during the first year of the second extended mission, and both the altitude and latitude of periapsis decreased progressively under the influence of the gravitational pull of the Sun. A series of four OCMs between June 2014 and December 2015 raised periapsis altitude and prolonged the mission duration.

During the final six weeks of the second extended mission, MESSENGER completed a low-altitude or "hover" campaign during which seven OCMs in March and April 2015 maintained the altitude at closest approach, relative to measured topography, between 5 and 37 km (McAdams et al., 2015). The campaign was unprecedented in several respects, including the short intervals between successive OCMs, the application of MLA altimetry data to validate trajectory solutions obtained by the project's mission design and navigation teams, and the use of propulsion system pressurant (helium gas) to impart thrust to the spacecraft during the final four OCMs once usable onboard hydrazine had been exhausted. After all usable pressurant as well as propellant had been consumed, no further OCMs were possible, and the spacecraft impacted Mercury's surface as expected on 30 April 2015. A plot of MESSENGER's closest-approach altitude during the hover campaign is shown in Figure 1.14.

All MESSENGER instruments continued to operate until the final transmission of data from the spacecraft, and by the end of MESSENGER's orbital operations all scientific objectives (Table 1.5) and project requirements (Table 1.6) for the second extended mission had been met. To illustrate this statement by example, we provide here an overview of some of the principal findings from the final two years of orbital observations, by scientific objective (Table 1.5). The full set of MESSENGER observations and their scientific implications for Mercury are described at greater length in the other chapters of this volume.

1.6.2.1 Recent Surface Processes

High-resolution images of hollows acquired at low elevations late in the second extended mission permitted measurements of the depths of hundreds of individual hollows; the results indicate an average depth of 24 ± 16 m and a range of values sufficiently narrow as to favor the hypothesis that hollows cease to increase in depth when a volatile-depleted lag deposit becomes sufficiently thick to protect the underlying surface (Blewett et al., 2016). Even the highest-resolution images reveal no superposed impact craters, implying that hollows are very young (Blewett et al., 2016). On the basis of the distribution of impact craters with high-reflectance ejecta, optical maturation or space weathering of surface material on Mercury is more rapid by a factor of as much as 4 than on the Moon (Braden and Robinson, 2013). Moreover, there are fewer optically immature craters per unit area on Mercury than on the Moon, indicating

Table 1.5. *Scientific objectives for MESSENGER's second extended mission.*

1.1 Investigate how hollows initiate and how they contribute to the exosphere.
1.2 Investigate how space weathering progressively modifies the optical properties of freshly exposed crustal materials.
1.3 Investigate how meteoritic materials contribute to the geochemistry of the surface.
2.1 Characterize how large-scale systems of lobate scarps spatially localize.
2.2 Determine whether there is evidence of recent contractional and extensional deformation.
2.3 Determine the crustal structure that is associated with contractional tectonics.
3.1 Investigate whether the northern plains are compositionally uniform.
3.2 Determine whether there are observable elemental and mineralogical differences between pyroclastic deposits and high-reflectance red plains.
3.3 Investigate the compositional relationship between low-reflectance blue plains and low-reflectance material.
3.4 Search for layers within plains units that could be volcanic flows.
3.5 Characterize the detailed nature of flow unit boundaries, and search for flow unit boundaries in the plains materials.
4.1 Characterize the morphology of small craters that host radar-bright material.
4.2 Determine which craters contain materials that are bright and dark at the wavelength (1064 nm) of the MLA and what physical features distinguish them.
4.3 Determine whether longitudinal variation of hydrogen concentrations within the north polar region is consistent with the distribution of radar-bright materials in permanently shadowed craters.
5.1 Determine fluences of protons, heavy ions, and electrons to the surface, and characterize how they vary with latitude and time.
5.2 Determine whether the signatures of particle precipitation to the surface are consistent with the inferred sources.
5.3 Determine what physical processes are revealed by the evolution of energetic electron events.
6.1 Characterize the nature of induced magnetic fields, and determine their effectiveness in controlling access of solar wind plasma to the surface.
6.2 Determine how the populations of heavy ions and protons in the cusps and the rest of the magnetosphere differ under extreme solar wind pressures.
6.3 Investigate how energetic electron events respond to increasing solar wind pressure or speed as well as prolonged stable solar wind, and determine whether exospheric density and distribution change under extreme conditions.
6.4 Characterize the time profiles of solar wind speed and density to which Mercury is exposed and how heliospheric pickup and suprathermal ions contribute to the exosphere.
6.5 Investigate how field-aligned currents close at low altitude.
7.1 Investigate how the lithosphere has evolved over time.
7.2 Characterize spatial variations in crustal thickness and density and determine the constraints these variations place on the history of crustal production.
7.3 Search for evidence of crustal magnetization, and evaluate the constraints that this evidence places on the evolution of the dynamo field.
7.4 Search for evidence of finite electrical conductivity of the mantle in induced magnetic field signatures and determine what constraints this evidence places on present mantle temperature structure.
7. 5 Discover the crustal geological characteristics and their variability with terrain types at small spatial scales not previously observable.

Table 1.6. *Project requirements for MESSENGER's second extended mission.*

1. Characterize faulted terrain by acquiring at least one of the following: (a) 20 NAC along-track stereo pairs or (b) 40 MLA topographic profiles.
2. Characterize fresh craters by acquiring at least one of the following: (a) 20 WAC 11-color image sets or (b) 20 NAC along-track stereo pairs.
3. Characterize hollows by acquiring (a) UVVS observations of exospheric species over eight clusters of hollows on three different dates and from two different viewing geometries per feature or (b) 20 along-track NAC stereo pairs and 20 11-color image sets each.
4. Characterize surface features at very high resolution by acquiring 750 NAC images at ≤10-m/pixel scale and 100 NAC images at ≤5-m/pixel scale
5. Search for color variations within the northern plains by acquiring 5-color MDIS images of 75% of the surface area north of 60°N at phase angles <60°.
6. Constrain the elemental composition of spectral end-member materials by acquiring targeted XRS spectra (a) from the large pyroclastic deposit northeast of Rachmaninoff and (b) of at least two different portions of low-reflectance blue plains exterior to the Caloris basin. For each target, acquire a minimum of 1000 s of spectral integration spread over at least five different orbits.

7. (a) Characterize MLA-bright and -dark materials by acquiring MLA ranging and reflectance data along portions of two orbits for which ground tracks cross each of 10 craters <20 km in diameter, and (b) characterize the north polar hydrogen distribution at high spatial resolution by acquiring NS measurements for 70% of the time that the spacecraft altitude is <150 km.
8. Characterize crustal structure at high resolution by acquiring Doppler tracking data for portions of 100 orbits at altitudes <100 km.
9. Characterize the structure of crustal magnetization at high resolution by acquiring MAG and FIPS observations along portions of 100 orbits at altitudes <50 km in the vicinity of the northern plains.
10. Characterize magnetospheric particle flows and pitch-angle distributions by acquiring a defined set of 970 EPPS measurements distributed across several different pointing scenarios.
11. Characterize the exospheric response to conditions during solar maximum and the declining phase of the solar cycle by acquiring a defined set of 5025 UVVS dayside and nightside observations, including searches for species with weaker resonant emissions.
12. Characterize the magnetospheric response to conditions during solar maximum and the declining phase of the solar cycle by acquiring MAG, EPPS, and NS/GRS observations for 75% of the time throughout the mission, including times at which the spacecraft altitude is <50 km.

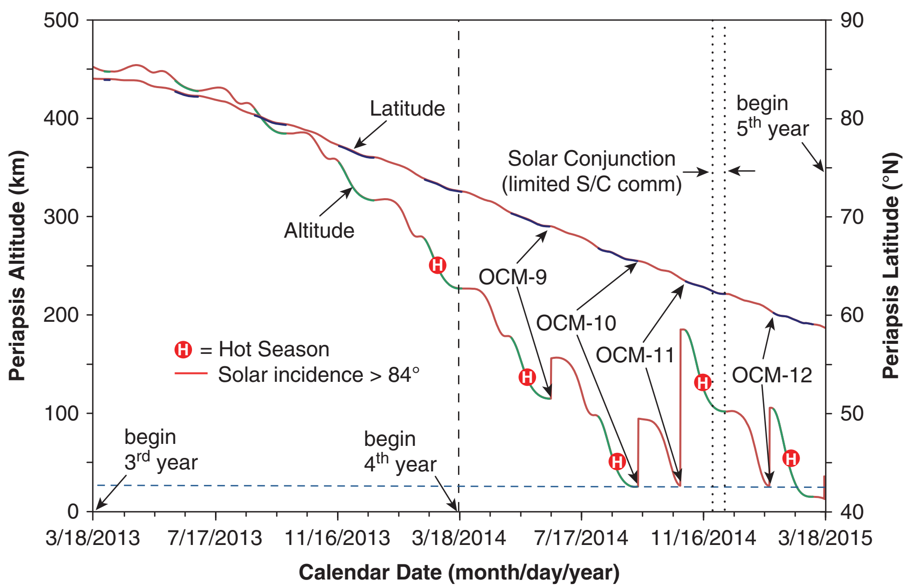

Figure 1.13. Evolution of the altitude and latitude of MESSENGER's periapsis during most of the second extended mission, from 18 March 2013 to 18 March 2015. Portions of the orbital observations when MESSENGER was in its "hot season" (near noon–midnight orbit configuration with periapsis on the dayside) are marked, as are periods when the solar incidence angle (measured from the vertical) along the dayside orbit track exceeded 84° and no imaging near periapsis was planned. A period of superior solar conjunction, when the spacecraft was on the opposite side of the Sun from Earth and thus communication with the spacecraft was limited, is indicated (S/C denotes spacecraft). From McAdams et al. (2014).

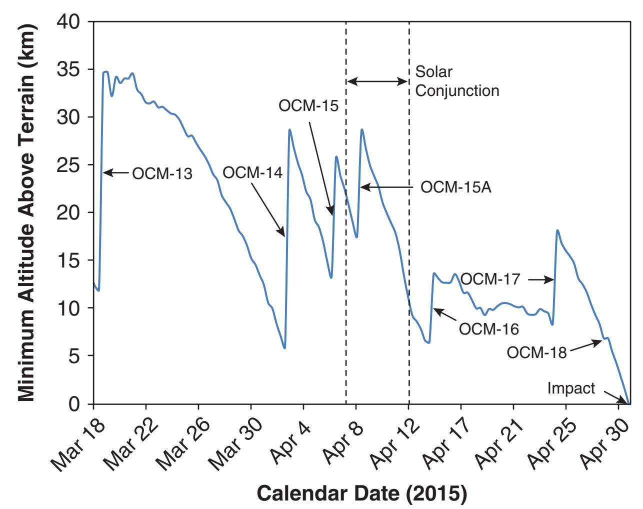

Figure 1.14. MESSENGER's altitude at closest approach, relative to measured topography, during the mission's hover campaign over the final six weeks of orbital operations. A period of superior solar conjunction, when the spacecraft was on the opposite side of the Sun from Earth, is indicated by vertical dashed lines. From McAdams et al. (2015).

that rayed craters on Mercury are younger on average than those on the Moon (Braden and Robinson, 2013).

1.6.2.2 Crustal Stress Field over Time

Images of Mercury's surface acquired from orbit by MESSENGER showed that the planet's global contraction involved a substantially greater number and variety of structures than previously recognized. The strain accommodated by identified tectonic features implies that Mercury contracted radially by as much as 7 km, well in excess of the 0.8–3 km previously reported from photogeological studies and resolving the long-standing discrepancy with the predictions of thermal history models (Byrne et al., 2014). Moreover, an additional 2 km of radial contraction may have been accommodated elastically prior to the development of widespread faulting (Klimczak, 2015). The distribution and orientation of tectonic features are consistent with scenarios in which tidal despinning accompanied the earliest phases of global contraction (Klimczak et al., 2015). That global contraction was underway within 1 Gyr of Mercury's formation is consistent with the cessation of widespread smooth plains formation around 3.5 Ga, given that lithospheric stresses characterized by horizontal compression would have inhibited the upward ascent of magma (Byrne et al., 2016). Crosscutting relations between lobate scarps and fresh craters indicate that contractional deformation on Mercury continued to geologically recent times (Banks et al., 2015).

1.6.2.3 Composition of Volcanic Materials over Time

The second extended mission doubled the opportunity to conduct elemental remote sensing of Mercury's surface over the primary and first extended missions. As the spatial resolution of such geochemical measurements improved, it became evident that Mercury's surface could be divided into approximately half a dozen geochemical terranes, each with distinctive compositional characteristics resolvable from several independent measurement types, including fluorescent X-rays (Weider et al., 2015), the flux of thermal neutrons (Peplowski et al., 2015), and the flux of fast neutrons (Lawrence et al., 2017). The chemical differences among terranes are broadly consistent with decreases in mantle potential temperature and degree of melting with time on Mercury (Namur et al., 2016).

1.6.2.4 Volatiles in the North Polar Region

During MESSENGER's second extended mission, images were acquired with the broadband clear filter on the MDIS WAC of persistently shadowed areas on the floors of impact craters at high northern latitudes (Chabot et al., 2014, 2016). On the floor of Prokofiev crater, a site previously identified on the basis of MLA reflectance measurements and thermal models as containing widespread surface water ice, the area in persistent shadow was seen to have a cratered texture that resembles the neighboring sunlit surface except for its uniformly higher reflectance, indicating that the surficial ice was emplaced after formation of the underlying craters (Chabot et al., 2014). In areas where water ice was inferred to be present from radar observations but covered by a thin layer of dark volatile material on the basis of MLA reflectance and thermal models, regions with uniformly low reflectance were seen to extend to the edges of the shadowed areas and terminate with sharp boundaries (Chabot et al., 2014). In images acquired during the low-altitude campaign late in the second extended mission, brightness variations across the low-reflectance deposits correlate with variations in the modeled biannual maximum surface temperature across the persistently shadowed regions, supporting the conclusion that multiple volatile organic compounds are present in addition to water ice (Chabot et al., 2016). Either a recent large impact by a comet or volatile-rich asteroid, or ongoing bombardment by volatile-rich micrometeoroids, could deliver water and volatile organic material to Mercury (Chabot et al., 2014, 2016).

1.6.2.5 Ion and Electron Precipitation

During MESSENGER's second extended mission, energetic electron events were characterized with data from multiple instruments, including measurements at high temporal resolution (10 ms) with the GRS ACS (Lawrence et al., 2015; Ho et al., 2016; Baker et al., 2016). The most energetic electron bursts detected by MESSENGER sensors appeared to be produced in the midnight sector of Mercury's magnetosphere, supporting the view that energetic electrons are accelerated in the near-tail region and are then injected onto closed magnetic field lines on the planetary nightside during substorm-like events (Baker et al., 2016). The electrons populate the plasma sheet and drift rapidly eastward toward the dawn and prenoon sectors, at times executing multiple complete drifts around the planet to form "quasi-trapped" populations (Lawrence et al., 2015; Ho et al., 2016; Baker et al., 2016). Observations of plasma in Mercury's magnetosphere show a north–south asymmetry on the nightside, with markedly lower fluxes at low altitudes in the northern hemisphere than at higher altitudes in the south on the same field line, an asymmetry consistent with particle loss to the southern hemisphere surface during bounce motion in Mercury's offset dipole magnetic field (Korth et al., 2014). Plasma measurements in Mercury's magnetospheric cusp show evidence of three processes: (1) direct inflow from the magnetosheath, (2) local production of planetary photoions and ions sputtered off the surface from solar wind impact that are then accelerated upward, and (3) flow of magnetosheath and magnetospheric plasma accelerated from dayside magnetic reconnection (Raines et al., 2014). During solar energetic particle events, FIPS measured fluxes of electrons at MeV energies equal to ~40% of their upstream values over Mercury's entire polar cap, indicating that space weathering of the surface by energetic electrons is not limited to the region of the cusp (Gershman et al., 2015).

1.6.2.6 Response of the Exosphere and Magnetosphere

MESSENGER magnetic field observations demonstrated the presence of electric currents that flow along magnetic lines of force toward and away from the planet above Mercury's northern hemisphere; such currents are analogous to Birkeland currents at Earth, but close not through an ionosphere but rather through the planet, radially through the low-conductivity outer silicate shell and laterally from dawn to dusk through more conductive material at depth (Anderson et al., 2014). Magnetic field observations over 15 Mercury years showed a small annual (88-day) variation in the planetary dipole moment, evidence that induced magnetic fields in Mercury's core act to oppose the decrease in subsolar magnetopause standoff distance with increasing solar wind ram pressure (Johnson et al., 2016). The shielding provided by induced currents is substantially offset, however, by the effects of dayside magnetic reconnection, which erodes magnetic flux from the dayside magnetosphere and can be particularly intense during extreme solar wind events (Imber et al., 2014; Slavin et al., 2014). Observations of frequent magnetic flux ropes in the cross-tail current sheet confirm the high rate of magnetic reconnection in that portion of the magnetosphere (DiBraccio et al., 2015).

1.6.2.7 New Insights from Low-Altitude Observations

The low periapsis altitudes during the second half of MESSENGER's second extended mission enabled a variety of discoveries. Magnetic field measurements obtained at altitudes less than 150 km demonstrated for the first time the presence of crustal magnetic fields inferred to have been acquired by at least 3.9–3.7 Ga (Johnson et al., 2015). A magnetic dynamo must therefore have operated in Mercury's core early in the planet's history. The low altitudes also permitted NS observations to be made of large expanses of low-reflectance material and of the largest identified pyroclastic deposit on Mercury, northeast of the Rachmaninoff basin. An increase in thermal neutron flux over LRM compared with surrounding terrain (Peplowski et al., 2016) coupled with the material's distinctive reflectance characteristics (Murchie et al., 2015) point to graphite as a major darkening agent on Mercury and in LRM in particular. The preferential location of hollows in LRM and the higher than average concentration of graphite in that material suggests that hollow formation may involve loss of carbon, e.g., by ion sputtering or conversion to methane by proton irradiation (Blewett et al., 2016). A decrease in the thermal neutron flux over the large pyroclastic deposit (Peplowski et al., 2016) together with targeted XRS observations and spectral reflectance measurements indicate that the deposit is depleted in S (relative to Ca and Si) and C compared with Mercury's average surface, consistent with oxidation of graphite and sulfides during magma ascent, via reaction with oxides in the magma or assimilated country rock, and the formation of S- and C-bearing volatile species (Weider et al., 2016).

1.7 CONCLUSIONS AND OVERVIEW OF OTHER CHAPTERS

The MESSENGER mission met or exceeded all of its scientific objectives across a broad spectrum of planetary science disciplines, as well as all of its project requirements. The spacecraft completed orbital operations at Mercury over a period that was a factor of 4 longer than originally planned, despite radiation and thermal hazards particular to Mercury's distance from the Sun. As a result, we have markedly deepened our understanding of Mercury, its interaction with the local heliospheric environment, and its role as a member of the family of inner solar system planets.

The state of that understanding, as of the end of the MESSENGER mission, is laid out in the chapters that follow. Chapters 2–4 are on the bulk properties of Mercury: the chemical composition, the structure of the crust and lithosphere, and the deeper interior structure, respectively. Chapter 5 summarizes our knowledge of Mercury's magnetic field. Chapters 6–13 address Mercury's geology: its major geological units, its variations in surface elemental chemistry and inferred mineralogy, its spectral reflectance characteristics and their variation, its impact craters and cratering history, its tectonic features and deformational history, its volcanic features and magmatic history, its hollows, and its polar deposits, respectively. Chapters 14 and 15 deal with observations of Mercury's exosphere and models of the physical processes that govern exospheric behavior, respectively. Chapters 16 and 17 summarize our understanding of the structure and dynamics, respectively, of Mercury's magnetosphere. Chapters 18 and 19 address the formation and large-scale evolution, respectively, of the planet. The final chapter of the book, Chapter 20, gives an overview of the future exploration of Mercury, from a mission now nearing launch to concepts for follow-on missions in the more distant future.

REFERENCES

Aharonson, O., Zuber, M. T. and Solomon, S. C. (2004). Crustal remanence in an internally magnetized non-uniform shell: A possible source for Mercury's magnetic field? *Earth Planet. Sci. Lett.*, **218**, 261–268.

Anderson, B. J., Acuña, M. H., Lohr, D. A., Scheifele, J., Raval, A., Korth, H. and Slavin, J. A. (2007). The Magnetometer instrument on MESSENGER. *Space Sci. Rev.*, **131**, 417–450.

Anderson, B. J., Johnson, C. L., Korth, H., Purucker, M. E., Winslow, R. M., Slavin, J. A., Solomon, S. C., McNutt, R. L., Jr., Raines, J. M. and Zurbuchen, T. H. (2011a). The global magnetic field of Mercury from MESSENGER orbital observations. *Science*, **333**, 1859–1862.

Anderson, B. J., Perry, M. E., Choo, T. H., Steele, R. J., Nguyen, L., Lucks, M., Prockter, L. M., McNutt, R. L., Jr. and Solomon, S. C. (2011b). MESSENGER science observation planning for orbital operations at Mercury. *Lunar Planet. Sci.*, **42**, abstract 1862.

Anderson, B. J., Johnson, C. L., Korth, H., Winslow, R. M., Borovsky, J. E., Purucker, M. E., Slavin, J. A., Solomon, S. C., Zuber, M. T. and McNutt, R. L., Jr. (2012). Low-degree structure in Mercury's planetary magnetic field. *J. Geophys. Res.*, **117**, E00L12, doi:10.1029/2012JE004159.

Anderson, B. J., Johnson, C. L., Korth, H., Slavin, J. A., Winslow, R. M., Phillips, R. J., McNutt, R. L., Jr. and Solomon, S. C. (2014). Steady-state field-aligned currents at Mercury. *Geophys. Res. Lett.*, **41**, 7444–7452.

Anderson, J. D., Colombo, G., Esposito, P. B., Lau, E. L. and Trager, G. B. (1987). The mass, gravity field, and ephemeris of Mercury. *Icarus*, **71**, 337–349.

Andrews, G. B., Zurbuchen, T. H., Mauk, B. H., Malcom, H., Fisk, L. A., Gloeckler, G., Ho, G. C., Kelley, J. S., Koehn, P. L., LeFevere, T. W., Livi, S. S., Lundgren, R. A. and Raines, J. M. (2007). The Energetic Particle and Plasma Spectrometer instrument on the MESSENGER spacecraft. *Space Sci. Rev.*, **131**, 523–556.

Baker, D. N., Dewey, R. M., Lawrence, D. J., Goldsten, J. O., Peplowski, P. N., Korth, H., Slavin, J. A., Krimigis, S. M., Anderson, B. J., Ho, G. C., McNutt, R. L., Jr., Raines, J. M., Schriver, D. and Solomon, S. C. (2016). Intense energetic electron flux enhancements in Mercury's magnetosphere: An integrated view with high-resolution observations from MESSENGER. *J. Geophys. Res. Space Physics*, **121**, 2171–2184.

Balcerski, J. A., Hauck, S. A., II, Sun, P., Klimczak, C., Byrne, P. K., Phillips, R. J. and Solomon, S. C. (2013). New constraints on timing and mechanisms of regional tectonism from Mercury's tilted craters. *Lunar Planet. Sci.*, **44**, abstract 2444.

Banks, M. E., Xiao, Z., Watters, T. R., Strom, R. G., Braden, S. E., Chapman, C. R., Solomon, S. C., Klimczak, C. and Byrne, P. K. (2015). Duration of activity on lobate-scarp thrust faults on Mercury. *J. Geophys. Res. Planets*, **120**, 1751–1762.

Benz, W., Slattery, W. L. and Cameron, A. G. W. (1988). Collisional stripping of Mercury's mantle. *Icarus*, **74**, 516–528.

Berman, A. F., Domingue, D. L., Holdridge, M. E., Choo, T. H., Steele, R. J. and Shelton, R. G. (2010). Testing and validation of orbital operations plans for the MESSENGER mission. In *Observatory Operations: Strategies, Processes, and Systems III*, ed. D. R. Silva, A. B. Peck and B. T. Soifer. *Proc. SPIE*, 7737, doi:10.1117/12.857107.

Bida, T. A., Killen, R. M. and Morgan, T. H. (2000). Discovery of calcium in Mercury's atmosphere. *Nature*, **404**, 159–161.

Blewett, D. T., Chabot, N. L., Denevi, B. W., Ernst, C. M., Head, J. W., Izenberg, N. R., Murchie, S. L., Solomon, S. C., Nittler, L. R., McCoy, T. J., Xiao, Z., Baker, D. M. H., Fassett, C. I., Braden, S. E., Oberst, J., Scholten, F., Preusker, F. and Hurwitz, D. M. (2011). Hollows on Mercury: MESSENGER evidence for geologically recent volatile-related activity. *Science*, **333**, 1856–1859.

Blewett, D. T., Vaughan, W. M., Xiao, Z., Chabot, N. L., Denevi, B. W., Ernst, C. M., Helbert, J., D'Amore, M., Maturilli, A., Head, J. W. and Solomon, S. C. (2013). Mercury's hollows: Constraints on formation and composition from analysis of geological setting and spectral reflectance. *J. Geophys. Res. Planets*, **118**, 1013–1032.

Blewett, D. T., Stadermann, A. C., Susorney, H. C., Ernst, C. M., Xiao, Z., Chabot, N. L., Denevi, B. W., Murchie, S. L., McCubbin, F. M., Kinczyk, M. J., Gillis-Davis, J. J. and Solomon, S. C. (2016). Analysis of MESSENGER high-resolution images of Mercury's hollows and implications for hollow formation. *J. Geophys. Res. Planets*, **121**, 1798–1813.

Boardsen, S. A., Slavin, J. A., Anderson, B. J., Korth, H., Schriver, D. and Solomon, S. C. (2012). Survey of coherent ~1 Hz waves in Mercury's inner magnetosphere. *J. Geophys. Res.*, **117**, A00M05, doi:10.1029/2012JA017822.

Braden, S. E. and Robinson, M. S. (2013). Relative rates of optical maturation of regolith on Mercury and the Moon. *J. Geophys. Res. Planets*, **118**, 1903–1914.

Broadfoot, A. L., Shemanski, D. E. and Kumar, S. (1976). Mariner 10: Mercury atmosphere. *Geophys. Res. Lett.*, **3**, 577–580.

Burger, M. H., Killen, R. M., McClintock, W. E., Vervack, R. J., Jr., Merkel, A. W., Sprague, A. L. and Sarantos, M. (2012). Modeling MESSENGER observations of calcium in Mercury's exosphere. *J. Geophys. Res.*, **117**, E00L11, doi:10.1029/2012JE004158.

Burger, M. H., Killen, R. M., McClintock, W. E., Merkel, A. W., Vervack, R. J., Jr., Cassidy, T. A. and Sarantos, M. (2014). Seasonal variations in Mercury's dayside calcium exosphere. *Icarus*, **238**, 51–58.

Byrne, P. K., Watters, T. R., Murchie, S. L., Klimczak, C., Solomon, S. C., Prockter, L. M. and Freed, A. M. (2012). A tectonic survey of the Caloris basin, Mercury. *Lunar Planet. Sci.*, **43**, abstract 1722.

Byrne, P. K., Klimczak, C., Williams, D. A., Hurwitz, D. M., Solomon, S. C., Head, J. W., Preusker, F. and Oberst, J. (2013). An assemblage of surface lava flow features on Mercury. *J. Geophys. Res. Planets*, **118**, 1303–1322.

Byrne, P. K., Klimczak, C., Şengör, A. M. C., Solomon, S. C., Watters, T. R. and Hauck, S. A., II (2014). Mercury's global contraction much greater than earlier estimates. *Nature Geosci.*, **7**, 301–307.

Byrne, P. K., Ostrach, L. R., Fassett, C. I., Chapman, C. R., Denevi, B. W., Evans, A. J., Klimczak, C., Banks, M. E., Head, J. W. and Solomon, S. C. (2016). Widespread effusive volcanism on Mercury likely ended by about 3.5 Ga. *Geophys. Res. Lett.*, **43**, 7408–7416.

Cameron, A. G. W. (1985). The partial volatilization of Mercury. *Icarus*, **64**, 285–294.

Cassidy, T. A., Merkel, A. W., Burger, M. H., Sarantos, M., Killen, R. M., McClintock, W. E. and Vervack, R. J., Jr. (2015). Mercury's seasonal sodium exosphere: MESSENGER orbital observations. *Icarus*, **248**, 547–559.

Cavanaugh, J. F., Smith, J. C., Sun, X., Bartels, A. E., Ramos-Izquierdo, L., Krebs, D. J., McGarry, J. F., Trunzo, R., Novo-Gradac, A. M., Britt, J. L., Karsh, J., Katz, R. B., Lukemire, A., Szymkiewicz, R., Berry, D. L., Swinski, J. P., Neumann, G. A., Zuber, M. T. and Smith, D. E. (2007). The Mercury Laser Altimeter instrument for the MESSENGER mission. *Space Sci. Rev.*, **131**, 451–480.

Chabot, N. L., Ernst, C. M., Denevi, B. W., Harmon, J. K., Murchie, S. L., Blewett, D. T., Solomon, S. C. and Zhong, E. D. (2012). Areas of permanent shadow in Mercury's south polar region ascertained by MESSENGER orbital imaging. *Geophys. Res. Lett.*, **39**, L09204, doi:10.1029/2012GL051526.

Chabot, N. L., Ernst, C. M., Harmon, J. K., Murchie, S. L., Solomon, S. C., Blewett, D. T. and Denevi, B. W. (2013). Craters hosting radar-bright deposits in Mercury's north polar region: Areas of persistent shadow determined from MESSENGER images. *J. Geophys. Res. Planets*, **118**, 26–36.

Chabot, N. L., Ernst, C. M., Denevi, B. W., Nair, H., Deutsch, A. N., Blewett, D. T., Murchie, S. L., Neumann, G. A., Mazarico, E., Paige, D. A., Harmon, J. K., Head, J. W. and Solomon, S. C. (2014). Images of surface volatiles in Mercury's polar craters acquired by the MESSENGER spacecraft. *Geology*, **12**, 1051–1064.

Chabot, N. L., Ernst, C. M., Paige, D. A., Nair, H., Denevi, B. W., Blewett, D. T., Murchie, S. L., Deutsch, A. N., Head, J. W. and Solomon, S. C. (2016). Imaging Mercury's polar deposits during MESSENGER's low-altitude campaign. *Geophys. Res. Lett.*, **43**, 9461–9468.

Choo, T. H., Murchie, S. L., Bedini, P. D., Steele, R. J., Skura, J. P., Nguyen, L., Nair, H., Lucks, M., Berman, A. F., McGovern, J. A. and Turner, F. S. (2014). SciBox: An end-to-end automated science planning and commanding system. *Acta Astronaut.*, **93**, 490–496.

Christensen, U. R. (2006). A deep dynamo generating Mercury's magnetic field. *Nature*, **444**, 1056–1058.

COMPLEX (Committee on Lunar and Planetary Exploration) (1978). *Strategy for Exploration of the Inner Planets: 1977–1987*. Washington, DC: National Research Council, 105 pp.

Connerney, J. E. P. and Ness, N. F. (1988). Mercury's magnetic field and interior. In *Mercury*, ed. F. Vilas, C. R. Chapman and M. S. Matthews. Tucson, AZ: University of Arizona Press, pp. 479–488.

Denevi, B. W., Robinson, M. S., Solomon, S. C., Murchie, S. L., Blewett, D. T., Domingue, D. L., McCoy, T. J., Ernst, C. M., Head, J. W., Watters, T. R. and Chabot, N. L. (2009). The evolution of Mercury's crust: A global perspective from MESSENGER. *Science*, **324**, 613–618.

Denevi, B. W., Ernst, C. M., Meyer, H. M., Robinson, M. S., Murchie, S. L., Whitten, J. L., Head, J. W., Watters, T. R., Solomon, S. C., Ostrach, L. R., Chapman, C. R., Byrne, P. K. and Peplowski, P. N. (2013). The distribution and origin of smooth plains on Mercury. *J. Geophys. Res. Planets*, **118**, 891–907.

DiBraccio, G. A., Slavin, J. A., Boardsen, S. A., Anderson, B. J., Korth, H., Zurbuchen, T. H., Raines, J. M., Baker, D. N., McNutt, R. L., Jr. and Solomon, S. C. (2013). MESSENGER observations of magnetopause structure and dynamics at Mercury. *J. Geophys. Res. Space Physics*, **118**, 997–1008.

DiBraccio, G. A., Slavin, J. A., Imber, S. M., Gershman, D. J., Raines, J. M., Jackman, C. M., Boardsen, S. A., Anderson, B. J., Korth, H., Zurbuchen, T. H., McNutt, R. L., Jr. and Solomon, S. C. (2015). MESSENGER observations of flux ropes in Mercury's magnetotail. *Planet. Space Sci.*, **115**, 77–89.

Domingue, D. L., Koehn, P. L., Killen, R. M., Sprague, A. L., Sarantos, M., Cheng, A. F., Bradley, E. T. and McClintock, W. E. (2007). Mercury's atmosphere: A surface-bounded exosphere. *Space Sci. Rev.*, **131**, 161–186.

Dunne, J. A. and Burgess E. (1978). *The Voyage of Mariner 10: Mission to Venus and Mercury*. Special Publication SP-424. Washington, DC: NASA Scientific and Technical Information Office.

Evans, L. G., Peplowski, P. N., Rhodes, E. A., Lawrence, D. J., McCoy, T. J., Nittler, L. R., Solomon, S. C., Sprague, A. L., Stockstill-Cahill, K. R., Starr, R. D., Weider, S. Z., Boynton, W. V. and

Hamara, D. K. (2012). Major-element abundances on the surface of Mercury: Results from the MESSENGER Gamma-Ray Spectrometer. *J. Geophys. Res.*, **117**, E00L07, doi:10.1029/2012JE004178.

Evans, L. G., Peplowski, P. N., McCubbin, F. M., McCoy, T. J., Nittler, L. R., Zolotov, M. Yu., Ebel, D. S., Lawrence, D. J., Starr, R. D., Weider, S. Z. and Solomon, S. C. (2015). Chlorine on the surface of Mercury: MESSENGER gamma-ray measurements and implications for the planet's formation and evolution. *Icarus*, **257**, 417–427.

Fassett, C. I., Head, J. W., Baker, D. M. H., Zuber, M. T., Smith, D. E., Neumann, G. A., Solomon, S. C., Strom, R. G., Chapman, C. R., Prockter, L. M., Phillips, R. J., Oberst, J. and Preusker, F. (2012). Large impact basins on Mercury: Global distribution, characteristics and modification history from MESSENGER orbital data. *J. Geophys. Res.*, **117**, E00L08, doi:10.1029/2012JE004154.

Freed, A. M., Blair, D. M., Watters, T. R., Klimczak, C., Byrne, P. K., Solomon, S. C., Zuber, M. T. and Melosh, H. J. (2012). On the origin of graben and ridges within and near volcanically buried craters and basins in Mercury's northern plains. *J. Geophys. Res.*, **117**, E00L06, doi:10.1029/2012JE004119.

Gershman, D. J., Raines, J. M., Slavin, J. A., Zurbuchen, T. H., Anderson, B. J., Korth, H., Ho, G. C., Boardsen, S. A., Cassidy, T. A., Walsh, B. M. and Solomon, S. C. (2015). MESSENGER observations of solar energetic electrons within Mercury's magnetosphere. *J. Geophys. Res. Space Physics*, **120**, 8559–8571.

Giampieri, G. and Balogh, A. (2002). Mercury's thermoelectric dynamo model revisited. *Planet. Space Sci.*, **50**, 757–762.

Gold, R. E., Solomon, S. C., McNutt, R. L., Jr., Santo, A. G., Abshire, J. B., Acuña, M. H., Afzal, R. S., Anderson, B. J., Andrews, G. B., Bedini, P. D., Cain, J., Cheng, A. F., Evans, L. G., Feldman, W. C., Follas, R. B., Gloeckler, G., Goldsten, J. O., Hawkins, S. E., III, Izenberg, N. R., Jaskulek, S. E., Ketchum, E. A., Lankton, M. R., Lohr, D. A., Mauk, B. H., McClintock, W. E., Murchie, S. L., Schlemm, C. E., II, Smith, D. E., Starr, R. D. and Zurbuchen, T. H. (2001). The MESSENGER mission to Mercury: Scientific payload. *Planet. Space Sci.*, **49**, 1467–1479.

Goldsten, J. O., Rhodes, E. A., Boynton, W. V., Feldman, W. C., Lawrence, D. J., Trombka, J. I., Smith, D. M., Evans, L. G., White, J., Madden, N. W., Berg, P. C., Murphy, G. A., Gurnee, R. S., Strohbehn, K., Williams, B. D., Schaefer, E. D., Monaco, C. A., Cork, C. P., Eckels, J. D., Miller, W. O., Burks, M. T., Hagler, L. B., Deteresa, S. J. and Witte, M. C. (2007). The MESSENGER Gamma-Ray and Neutron Spectrometer. *Space Sci. Rev.*, **131**, 339–391.

Goudge, T. A., Head, J. W., Kerber, L., Blewett, D. T., Denevi, B. W., Domingue, D. L., Gillis-Davis, J. J., Gwinner, K., Helbert, J., Holsclaw, G. M., Izenberg, N. R., Klima, R. L., McClintock, W. E., Murchie, S. L., Neumann, G. A., Smith, D. E., Strom, R. G., Xiao, Z., Zuber, M. T. and Solomon, S. C. (2014). Global inventory and characterization of pyroclastic deposits on Mercury: New insights into pyroclastic activity from MESSENGER orbital data. *J. Geophys. Res. Planets*, **119**, 635–658.

Harmon, J. K. and Slade, M. A. (1992). Radar mapping of Mercury: Full-disk images and polar anomalies. *Science*, **258**, 640–643.

Harmon, J. K., Slade, M. A. and Rice, M. S. (2011). Radar imagery of Mercury's putative polar ice: 1999–2005 Arecibo results. *Icarus*, **211**, 37–50.

Hauck, S. A., II, Margot, J.-L., Solomon, S. C., Phillips, R. J., Johnson, C. L., Lemoine, F. G., Mazarico, E., McCoy, T. J., Padovan, S., Peale, S. J., Perry, M. E., Smith, D. E. and Zuber, M. T. (2013). The curious case of Mercury's internal structure. *J. Geophys. Res. Planets*, **118**, 1204–1220.

Hawkins, S. E., III, Boldt, J. D., Darlington, E. H., Espiritu, R., Gold, R. E., Gotwols, B., Grey, M. P., Hash, C. D., Hayes, J. R., Jaskulek, S. E., Kardian, C. J., Keller, M. R., Malaret, E. R., Murchie, S. L., Murphy, P. K., Peacock, K., Prockter, L. M., Reiter, R. A., Robinson, M. S., Schaefer, E. D., Shelton, R. G., Sterner, R. E., II, Taylor, H. W., Watters, T. R. and Williams, B. D. (2007). The Mercury Dual Imaging System on the MESSENGER spacecraft. *Space Sci. Rev.*, **131**, 247–338.

Head, J. W., Murchie, S. L., Prockter, L. M., Robinson, M. S., Solomon, S. C., Strom, R. G., Chapman, C. R., Watters, T. R., McClintock, W. E., Blewett, D. T. and Gillis-Davis, J. J. (2008). Volcanism on Mercury: Evidence from the first MESSENGER flyby. *Science*, **321**, 69–72.

Head, J. W., Chapman, C. R., Strom, R. G., Fassett, C. I., Denevi, B. W., Blewett, D. T., Ernst, C. M., Watters, T. R., Solomon, S. C., Murchie, S. L., Prockter, L. M., Chabot, N. L., Gillis-Davis, J. J., Whitten, J. L., Goudge, T. A., Baker, D. M. H., Hurwitz, D. M., Ostrach, L. R., Xiao, Z., Merline, W. J., Kerber, L., Dickson, J. L., Oberst, J., Byrne, P. K., Klimczak, C. and Nittler, L. R. (2011). Flood volcanism in the northern high latitudes of Mercury revealed by MESSENGER. *Science*, **333**, 1853–1856.

Helbert, J., Maturilli, A. and D'Amore, M. (2013). Visible and near infrared reflectance spectra of thermally processed synthetic sulfide as a potential analog for the hollow forming materials on Mercury. *Earth Planet. Sci. Lett.*, **369–370**, 233–238.

Ho, G. C., Krimigis, S. M., Gold, R. E., Baker, D. N., Slavin, J. A., Anderson, B. J., Korth, H., Starr, R. D., Lawrence, D. J., McNutt, R. L., Jr. and Solomon, S. C. (2011). MESSENGER observations of transient bursts of energetic electrons in Mercury's magnetosphere. *Science*, **333**, 1866–1868.

Ho, G. C., Krimigis, S. M., Gold, R. E., Baker, D. N., Anderson, B. J., Korth, H., Slavin, J. A., McNutt, R. L., Jr., Winslow, R. M. and Solomon, S. C. (2012). Spatial distribution and spectral characteristics of energetic electrons in Mercury's magnetosphere. *J. Geophys. Res.*, **117**, A00M04, doi:10.1029/2012JA017983.

Ho, G. C., Starr, R. D., Krimigis, S. M., Vandegriff, J. D., Baker, D. N., Gold, R. E., Anderson, B. J., Korth, H., Schriver, D., McNutt, R. L., Jr. and Solomon, S. C. (2016). MESSENGER observations of suprathermal electrons in Mercury's magnetosphere. *Geophys. Res. Lett.*, **43**, 550–555.

Hunten, D. M. and Sprague, A. L. (2002). Diurnal variation of sodium and potassium at Mercury. *Meteorit. Planet. Sci.*, **37**, 1191–1195.

Hurwitz, D. M., Head, J. W., Byrne, P. K., Xiao, Z., Solomon, S. C., Zuber, M. T., Smith, D. E. and Neumann, G. A. (2013). Investigating the origin of candidate lava channels on Mercury with MESSENGER data: Theory and observations. *J. Geophys. Res. Planets*, **118**, 471–486.

Imber, S. M., Slavin, J. A., Boardsen, S. A., Anderson, B. J., Korth, H., McNutt, R. L., Jr. and Solomon, S. C. (2014). MESSENGER observations of large dayside flux transfer events: Do they drive Mercury's substorm cycle? *J. Geophys. Res. Space Physics*, **119**, 5613–5623.

Johnson, C. L., Purucker, M. E., Korth, H., Anderson, B. J., Winslow, R. M., Al Asad, M. M. H., Slavin, J. A., Alexeev, I., Phillips, R. J., Zuber, M. T. and Solomon, S. C. (2012). MESSENGER observations of Mercury's magnetic field structure. *J. Geophys. Res.*, **117**, E00L14, doi:10.1029/2012JE004217.

Johnson, C. L., Phillips, R. J., Purucker, M. E., Anderson, B. J., Byrne, P. K., Denevi, B. W., Feinberg, J. M., Hauck, S. A., II, Head, J. W., III, Korth, H., James, P. B., Mazarico, E., Neumann, G. A., Philpott, L. C., Siegler, M. A., Tsyganenko, N. A. and Solomon, S. C. (2015). Low-altitude magnetic field measurements by MESSENGER reveal Mercury's ancient crustal field. *Science*, **348**, 892–895.

Johnson, C. L., Philpott, L. C., Anderson, B. J., Korth, H., Hauck, S. A., II, Heyner, D., Phillips, R. J., Winslow, R. M. and Solomon, S. C.

(2016). MESSENGER observations of induced magnetic fields in Mercury's core. *Geophys. Res. Lett*., **43**, 2436–2444.

Kerber, L., Head, J. W., Solomon, S. C., Murchie, S. L., Blewett, D. T. and Wilson, L. (2009). Explosive volcanic eruptions on Mercury: Eruption conditions, magma volatile content, and implications for interior volatile abundances. *Earth Planet. Sci. Lett*., **285**, 263–271.

Killen, R. M. and Ip, W.-H. (1999). The surface-bounded atmospheres of Mercury and the Moon. *Rev. Geophys*., **37**, 361–406.

Killen, R. M., Burger, M. H., Cassidy, T. A., Sarantos, M., Vervack, R. J., Jr., McClintock, W. E., Merkel, A. W., Sprague, A. L. and Solomon, S. C. (2012). Mercury's Na exosphere from MESSENGER data. *Bull. Amer. Astron. Soc*., **44**, abstract 401.01.

Klimczak, C. (2015). Limits on the brittle strength of planetary lithospheres undergoing global contraction. *J. Geophys. Res. Planets*, **120**, 2135–2151.

Klimczak, C., Watters, T. R., Ernst, C. M., Freed, A. M., Byrne, P. K., Solomon, S. C., Blair, D. M. and Head, J. W. (2012). Deformation associated with ghost craters and basins in volcanic smooth plains on Mercury: Strain analysis and implications for plains evolution. *J. Geophys. Res*., **117**, E00L03, doi:10.1029/2012JE004100.

Klimczak, C., Ernst, C. M., Byrne, P. K., Solomon, S. C., Watters, T. R., Murchie, S. L., Preusker, F. and Balcerski, J. A. (2013). Insights into the subsurface structure of the Caloris basin, Mercury, from assessments of mechanical layering and changes in long-wavelength topography. *J. Geophys. Res. Planets*, **118**, 2030–2044.

Klimczak, C., Byrne, P. K. and Solomon, S. C. (2015). A rock-mechanical assessment of Mercury's global tectonic fabric. *Earth Planet. Sci. Lett*., **416**, 82–90.

Koehn, P. L., Zurbuchen, T. H., Gloeckler, G., Lundgren, R. A. and Fisk, L. A. (2002). Measuring the plasma environment at Mercury: The Fast Imaging Plasma Spectrometer. *Meteorit. Planet. Sci*., **37**, 1173–1189.

Korth, H., Anderson, B. J., Raines, J. M., Slavin, J. A., Zurbuchen, T. H., Johnson, C. L., Purucker, M. E., Winslow, R. M., Solomon, S. C. and McNutt, R. L., Jr. (2011). Plasma pressure in Mercury's equatorial magnetosphere derived from MESSENGER Magnetometer observations. *Geophys. Res. Lett*., **38**, L22201, doi:10.1029/2011GL049451.

Korth, H., Anderson, B. J., Johnson, C. L., Winslow, R. M., Slavin, J. A., Purucker, M. E., Solomon, S. C. and McNutt, R. L., Jr. (2012). Characteristics of the plasma distribution in Mercury's equatorial magnetosphere derived from MESSENGER Magnetometer observations. *J. Geophys. Res*., **117**, A00M07, doi:10.1029/2012JA018052.

Korth, H., Anderson, B. J., Gershman, D. J., Raines, J. M., Slavin, J. A., Zurbuchen, T. H., Solomon, S. C. and McNutt, R. L., Jr. (2014). Plasma distribution in Mercury's magnetosphere derived from MESSENGER Magnetometer and Fast Imaging Plasma Spectrometer observations. *J. Geophys. Res. Space Physics*, **119**, 2917–2932.

Lawrence, D. J., Feldman, W. C., Goldsten, J. O., Maurice, S., Peplowski, P. N., Anderson, B. J., Bazell, D., McNutt, R. L., Jr., Nittler, L. R., Prettyman, T. H., Rodgers, D. J., Solomon, S. C. and Weider, S. Z. (2013). Evidence for water ice near Mercury's north pole from MESSENGER Neutron Spectrometer measurements. *Science*, **339**, 292–296.

Lawrence, D. J., Anderson, B. J., Baker, D. N., Feldman, W. C., Ho, G. C., Korth, H., McNutt, R. L., Jr., Peplowski, P. N., Solomon, S. C., Starr, R. D. Vandegriff, J. D. and Winslow, R. M. (2015). Comprehensive survey of energetic electron events in Mercury's magnetosphere with data from the MESSENGER Gamma-Ray and Neutron Spectrometer. *J. Geophys. Space Physics*, **120**, 2851–2876.

Lawrence, D. J., Peplowski, P. N., Beck, A. W., Feldman, W. C., Frank, E. A., McCoy, T. J., Nittler, L. R. and Solomon, S. C. (2017). Compositional terranes on Mercury: Information from fast neutrons. *Icarus*, **281**, 32–45.

Leary, J. C., Conde, R. F., Dakermanji, G., Engelbrecht, C. S., Ercol, C. J., Fielhauer, K. B., Grant, D. G., Hartka, T. J., Hill, T. A., Jaskulek, S. E., Mirantes, M. A., Mosher, L. E., Paul, M. V., Persons, D. F., Rodberg, E. H., Srinivasan, D. K., Vaughan, R. M. and Wiley, S. R. (2007). The MESSENGER spacecraft. *Space Sci. Rev*., **131**, 187–217.

Leblanc, F. and Johnson, R. E. (2003). Mercury's sodium exosphere. *Icarus*, **164**, 261–281.

Lewis, J. S. (1988). Origin and composition of Mercury. In *Mercury*, ed. F. Vilas, C. R. Chapman, and M. S. Matthews. Tucson, AZ: University of Arizona Press, pp. 651–669.

Margot, J.-L., Peale, S. J., Jurgens, R. F., Slade, M. A. and Holin, I. V. (2007). Large longitude libration of Mercury reveals a molten core. *Science*, **316**, 710–714.

Margot, J.-L., Peale, S. J., Solomon, S. C., Hauck, S. A., II, Ghigo, F. D., Jurgens, R. F., Yseboodt, M., Giorgini, J. D., Padovan, S. and Campbell, D. B. (2012). Mercury's moment of inertia from spin and gravity data. *J. Geophys. Res*., **117**, E00L09, doi:10.1029/2012JE004161.

McAdams, J. V., Dunham, D. W., Farquhar, R. W., Taylor, A. H. and Williams, B. G. (2005). Trajectory design and maneuver strategy for the MESSENGER mission to Mercury. *Spaceflight Mechanics 2005, Adv. Astronaut. Sci.*, **120**, Part II, 1185–1204.

McAdams, J. V., Farquhar, R. W., Taylor, A. H. and Williams, B. G. (2007). MESSENGER mission design and navigation. *Space Sci. Rev*., **131**, 219–246.

McAdams, J. V., Moessner, D. P., Williams, K. E., Taylor, A. H., Page, B. R. and O'Shaughnessy, D. J. (2011). MESSENGER – Six primary maneuvers, six planetary flybys, and 6.6 years to Mercury orbit. *Astrodynamics 2011: Part III, Adv. Astronaut. Sci.*, **142**, 2191–2210.

McAdams, J. V., Solomon, S. C., Bedini, P. D., Finnegan, E. J., McNutt, R. L., Jr., Calloway, A. B., Moessner, D. P., Wilson, M. W., Gallagher, D. T., Ercol, C. J. and Flanigan, S. H. (2012). MESSENGER at Mercury: From orbit insertion to first extended mission. Presented at the *63rd International Astronautical Congress*, paper IAC-12-C1.5.6, 11 pp., Naples, Italy, 1–5 October.

McAdams, J. V., Bryan, C. G., Moessner, D. P., Page, B. R., Stanbridge, D. R. and Williams, K. E. (2014). Orbit design and navigation through the end of MESSENGER's extended mission at Mercury. *Space Flight Mechanics 2014: Part III, Adv. Astronaut. Sci*., **152**, 2299–2318.

McAdams, J. V., Bryan, C. G., Bushman, S. S., Calloway, A. B., Carranza, E., Flanigan, S. H., Kirk, M. N., Korth, H., Moessner, D. P., O'Shaughnessy, D. J. and Williams, K. E. (2015). Engineering MESSENGER's grand finale at Mercury: The low-altitude hover campaign. *Astrodynamics Specialist Conference,* American Astronautical Society, paper AAS 15–634, 20 pp., Vail, CO., 9–13 August.

McClintock, W. E. and Lankton, M. R. (2007). The Mercury Atmospheric and Surface Composition Spectrometer for the MESSENGER mission. *Space Sci. Rev*., **131**, 481–522.

McNutt, R. L., Jr., Solomon, S. C., Gold, R. E., Leary, J. C. and the MESSENGER team (2006). The MESSENGER mission to Mercury: Development history and early mission status. *Adv. Space Res*., **38**, 564–571.

Merkel, A. W., McClintock, W. E., Sarantos, M., Cassidy, T. A., Vervack, R. J., Jr., Burger, M. H., Killen, R. M., Sprague, A. L. and Solomon, S. C. (2012). Seasonal variability and local time dependence of Mercury's dayside magnesium exosphere.

Presented at 2012 Fall Meeting, American Geophysical Union, abstract P33B-1929, San Francisco, CA, 3–7 December.

Merkel, A. W., Cassidy, T. A., Vervack, R. J., Jr., McClintock, W. E., Sarantos, M., Burger, M. H. and Killen, R. M. (2017). Seasonal variations of Mercury's magnesium dayside exosphere from MESSENGER observations. *Icarus*, **281**, 46–54.

Moses, J. I., Rawlins, K., Zahnle, K. and Dones, L. (1999). External sources of water for Mercury's putative ice deposits. *Icarus*, **137**, 197–221.

Murchie, S. L., Klima, R. L., Denevi, B. W., Ernst, C. M., Keller, M. R., Domingue, D. L., Blewett, D. T., Chabot, N. L., Hash, C. D., Malaret, E., Izenberg, N. R., Vilas, F., Nittler, L. R., Gillis-Davis, J. J., Head, J. W. and Solomon, S. C. (2015). Orbital multispectral mapping of Mercury with the MESSENGER Mercury Dual Imaging System: Evidence for the origins of plains units and low-reflectance material. *Icarus*, **254**, 287–305.

Namur, O., Collinet, M., Charlier, B., Grove, T. L., Holtz, F. and McCammon, C. (2016). Melting processes and mantle sources of lavas on Mercury. *Earth Planet. Sci. Lett*., **439**, 117–128.

Ness, N. F., Behannon, K. W., Lepping, R. P. and Whang, Y. C. (1976). Observations of Mercury's magnetic field. *Icarus*, **28**, 479–488.

Neumann, G. A., Cavanaugh, J. F., Sun, X., Mazarico, E. M., Smith, D. E., Zuber, M. T., Mao, D., Paige, D. A., Solomon, S. C., Ernst, C. M. and Barnouin, O. S. (2013). Bright and dark polar deposits on Mercury: Evidence for surface volatiles. *Science*, **339**, 296–300.

Nittler, L. R., Starr, R. D., Weider, S. Z., McCoy, T. J., Boynton, W. V., Ebel, D. S., Ernst, C. M., Evans, L. G., Goldsten, J. O., Hamara, D. K., Lawrence, D. J., McNutt, R. L., Jr., Schlemm, C. E., II, Solomon, S. C. and Sprague, A. L. (2011). The major-element composition of Mercury's surface from MESSENGER X-ray spectrometry. *Science*, **333**, 1847–1851.

Paige, D. A., Wood, S. E. and Vasavada, A. R. (1992). The internal stability of water ice at the poles of Mercury. *Science*, **258**, 643–646.

Paige, D. A., Siegler, M. A., Harmon, J. K., Neumann, G. A., Mazarico, E. M., Smith, D. E., Zuber, M. T., Harju, E., Delitsky, M. L. and Solomon, S. C. (2013). Thermal stability of volatiles in the north polar region of Mercury. *Science*, **339**, 300–303.

Peale, S. J. (1976). Does Mercury have a molten core? *Nature*, **262**, 765–766.

Peale, S. J., Phillips, R. J., Solomon, S. C., Smith, D. E. and Zuber, M. T. (2002). A procedure for determining the nature of Mercury's core. *Meteorit. Planet. Sci*., **37**, 1269–1283.

Peplowski, P. N., Evans, L. G., Hauck, S. A., II, McCoy, T. J., Boynton, W. V., Gillis-Davis, J. J., Ebel, D. S., Goldsten, J. O., Hamara, D. K., Lawrence, D. J., McNutt, R. L., Jr., Nittler, L. R., Solomon, S. C., Rhodes, E. A., Sprague, A. L., Starr, R. D. and Stockstill-Cahill, K. R. (2011). Radioactive elements on Mercury's surface from MESSENGER: Implications for the planet's formation and evolution. *Science*, **333**, 1850–1852.

Peplowski, P. N., Lawrence, D. J., Rhodes, E. A., Sprague, A. L., McCoy, T. J., Denevi, B. W., Evans, L. G., Head, J. W., Nittler, L. R., Solomon, S. C., Stockstill-Cahill, K. R. and Weider, S. Z. (2012). Variations in the abundances of potassium and thorium on the surface of Mercury: Results from the MESSENGER Gamma-Ray Spectrometer. *J. Geophys. Res*., **117**, E00L04, doi:10.1029/2012JE004141.

Peplowski, P. N., Lawrence, D. J., Feldman, W. C., Goldsten, J. O., Bazell, D., Evans, L. G., Head, J. W., Nittler, L. R., Solomon, S. C. and Weider, S. Z. (2015). Geochemical terranes of Mercury's northern hemisphere as revealed by MESSENGER neutron measurements. *Icarus*, **253**, 346–353.

Peplowski, P. N., Klima, R. L., Lawrence, D. J., Ernst, C. M., Denevi, B. W., Frank, E. A., Goldsten, J. O., Murchie, S. L., Nittler, L. R. and Solomon, S. C. (2016). Remote sensing evidence for an ancient carbon-bearing crust on Mercury. *Nature Geosci*., **9**, 273–276.

Potter, A. and Morgan, T. (1985). Discovery of sodium in the atmosphere of Mercury. *Science*, **229**, 651–653.

Potter, A. E. and Morgan, T. H. (1986). Potassium in the atmosphere of Mercury. *Icarus*, **67**, 336–340.

Preusker, F., Oberst, J., Head, J. W., Watters, T. R., Robinson, M. S., Zuber, M. T. and Solomon, S. C. (2011). Stereo topographic models of Mercury after three MESSENGER flybys. *Planet. Space Sci*., **59**, 1910–1917.

Prockter, L. M., Ernst, C. M., Denevi, B. W., Chapman, C. R., Head, J. W., Fassett, C. I., Merline, W. J., Solomon, S. C., Watters, T. R., Strom, R. G., Cremonese, G., Marchi, S. and Massironi, M. (2010). Evidence for young volcanism on Mercury from the third MESSENGER flyby. *Science*, **329**, 668–671.

Raines, J. M., Gershman, D. J., Zurbuchen, T. H., Sarantos, M., Slavin, J. A., Gilbert, J. A., Korth, H., Anderson, B. J., Gloeckler, G., Krimigis, S. M., Baker, D. N., McNutt, R. L., Jr. and Solomon, S. C. (2013). Distribution and compositional variations of plasma ions in Mercury's space environment: The first three Mercury years of MESSENGER observations. *J. Geophys. Res. Space Physics*, **118**, 1604–1619.

Raines, J. M., Gershman, D. J., Slavin, J. A., Zurbuchen, T. H., Korth, H., Anderson, B. J. and Solomon, S. C. (2014). Structure and dynamics of Mercury's magnetospheric cusp: MESSENGER measurements of protons and planetary ions. *J. Geophys. Res. Space Physics*, **119**, 6587–6602.

Robinson, M. S., Murchie, S. L., Blewett, D. T., Domingue, D. L., Hawkins, S. E., III, Head, J. W., Holsclaw, G. M., McClintock, W. E., McCoy, T. J., McNutt, R. L., Jr., Prockter, L. M. Solomon, S. C. and T. R. Watters, T. R. (2008). Reflectance and color variations on Mercury: Regolith processes and compositional heterogeneity. *Science*, **321**, 66–69.

Santo, A. G., Gold, R. E., McNutt, R. L., Jr., Solomon, S. C., Ercol, C. J., Farquhar, R. W., Hartka, T. J., Jenkins, J. E., McAdams, J. V., Mosher, L. E., Persons, D. F., Artis, D. A., Bokulic, R. S., Conde, R. F., Dakermanji, G., Goss, M. E., Jr., Haley, D. R., Heeres, K. J., Maurer, R. H., Moore, R. C., Rodberg, E. H., Stern, T. G., Wiley, S. R., Williams, B. G., Yen, C. L. and Peterson, M. R. (2001). The MESSENGER mission to Mercury: Spacecraft and mission design. *Planet. Space Sci*., **49**, 1481–1500.

Schlemm, C. E., II, Starr, R. D., Ho, G. C., Bechtold, K. E., Hamilton, S. A., Boldt, J. D., Boynton, W. V., Bradley, W., Fraeman, M. E., Gold, R. E., Goldsten, J. O., Hayes, J. R., Jaskulek, S. E., Rossano, E., Rumpf, R. A., Schaefer, E. D., Strohbehn, K., Shelton, R. G., Thompson, R. E., Trombka, J. I. and Williams, B. D. (2007). The X-Ray Spectrometer on the MESSENGER spacecraft. *Space Sci. Rev*., **131**, 393–415.

Schubert, G., Ross, M. N., Stevenson, D. J. and Spohn, T. (1988). Mercury's thermal history and the generation of its magnetic field. In *Mercury*, ed. F. Vilas, C. R. Chapman and M. S. Matthews. Tucson, AZ: University of Arizona Press, pp. 429–460.

Siegfried, R. W., II and Solomon, S. C. (1974). Mercury: Internal structure and thermal evolution. *Icarus*, **23**, 192–205.

Slade, M. A., Butler, B. J. and Muhleman, D. O. (1992). Mercury radar imaging: Evidence for polar ice. *Science*, **258**, 635–640.

Slavin, J. A., Acuña, M. A., Anderson, B. J., Baker, D. N., Benna, M., Gloeckler, G., Gold, R. E., Ho, G. C., Killen, R. M., Korth, H., Krimigis, S. A., McNutt, R. L., Jr., Nittler, L. R., Raines, J. M., Schriver, D., Solomon, S. C., Starr, R. D., Trávníček, P. and Zurbuchen, T. H. (2008). Mercury's magnetosphere after MESSENGER's first flyby. *Science*, 321, 85–89.

Slavin, J. A., Anderson, B. J., Baker, D. N., Benna, M., Boardsen, S. A., Gold, R. E., Ho, G. C., Imber, S. M., Korth, H., Krimigis, S. M., McNutt, R. L., Jr., Raines, J. M., Sarantos, M., Schriver, D., Solomon, S. C., Trávníček, P. and Zurbuchen, T. H. (2012a). MESSENGER and Mariner 10 flyby observations of magnetotail structure and dynamics at Mercury. *J. Geophys. Res*., **117**, A01215, doi:10.1029/2011JA016900.

Slavin, J. A., Imber, S. M., Boardsen, S. A., DiBraccio, G. A., Sundberg, T., Sarantos, M., Nieves-Chinchilla, T., Szabo, A., Anderson, B. J., Korth, H., Zurbuchen, T. H., Raines, J. M., Johnson, C. L., Winslow, R. M., Killen, R. M., McNutt, R. L., Jr. and Solomon, S. C. (2012b). MESSENGER observations of a flux-transfer-event shower at Mercury. *J. Geophys. Res*., **117**, A00M06, doi:10.1029/2012JA017926.

Slavin, J. A., DiBraccio, G. A., Gershman, D. J., Imber, S. M., Poh, G. K., Raines, J. M. Zurbuchen, T. H., Jia, X., Baker, D. N., Glassmeier, K.-H., Livi, S. A., Boardsen, S. A., Cassidy, T. A., Sarantos, M., Sundberg, T., Masters, A., Johnson, C. L., Winslow, R. M., Anderson, B. J., Korth, H., McNutt, R. L., Jr. and Solomon, S. C. (2014). MESSENGER observations of Mercury's dayside magnetosphere under extreme solar wind conditions. *J. Geophys. Res. Space Physics*, **119**, 8087–8116.

Smith, D. E., Zuber, M. T., Phillips, R. J., Solomon, S. C., Hauck, S. A., II, Lemoine, F. G., Mazarico, E., Neumann, G. A., Peale, S. J., Margot, J.-L., Johnson, C. L., Torrence, M. H., Perry, M. E., Rowlands, D. D., Goossens, S., Head, J. W. and Taylor, A. H. (2012). Gravity field and internal structure of Mercury from MESSENGER. *Science*, **336**, 214–217.

Solomon, S. C. (2003). Mercury: The enigmatic innermost planet. *Earth Planet. Sci. Lett*., **216**, 441–455.

Solomon, S. C., McNutt, R. L., Jr., Gold, R. E., Acuña, M. H., Baker, D. N., Boynton, W. V., Chapman, C. R., Cheng, A. F., Gloeckler, G., Head, J. W., III, Krimigis, S. M., McClintock, W. E., Murchie, S. L., Peale, S. J., Phillips, R. J., Robinson, M. S., Slavin, J. A., Smith, D. E., Strom, R. G., Trombka, J. I. and Zuber, M. T. (2001). The MESSENGER mission to Mercury: Scientific objectives and implementation. *Planet. Space Sci*., **49**, 1445–1465.

Sprague, A. L., Hunten, D. M. and Lodders, K. (1995). Sulfur at Mercury, elemental at the poles and sulfides in the regolith. *Icarus*, **118**, 211–215.

Sprague, A. L., Schmitt, W. J. and Hill, R. E. (1998). Mercury: Sodium atmosphere enhancements, radar-bright spots, and visible surface features. *Icarus*, **136**, 60–68.

Spudis, P. D. and Guest, J. E. (1988). Stratigraphy and geologic history of Mercury. In *Mercury*, ed. F. Vilas, C. R. Chapman and M. S. Matthews. Tucson, AZ: University of Arizona Press, pp. 118–164.

Srinivasan, D. K., Perry, M. E., Fielhauer, K. B., Smith, D. E. and Zuber, M. T. (2007). The radio frequency subsystem and radio science on MESSENGER. *Space Sci. Rev*., **131**, 557–571.

Srnka, L. J. (1976). Magnetic dipole moment of a spherical shell with TRM acquired in a field of internal origin. *Phys. Earth Planet. Inter*., **11**, 184–190.

Stanley, S., Bloxham, J., Hutchison, W. E. and Zuber, M. T. (2005). Thin shell dynamo models consistent with Mercury's weak observed magnetic field. *Earth Planet. Sci. Lett*., **234**, 27–38.

Starr, R. D., Schriver, D., Nittler, L. R., Weider, S. Z., Byrne, P. K., Ho, G. C., Rhodes, E. A., Schlemm, C. E., II, Solomon, S. C. and Trávníček, P. M. (2012). MESSENGER detection of electron-induced X-ray fluorescence from Mercury's surface. *J. Geophys. Res*., **117**, E00L02, doi:10.1029/2012JE004118.

Starukhina, L. (2001). Water detection on atmosphereless celestial bodies: Alternative explanations of the observations. *J. Geophys. Res*., **106**, 14701–14710.

Stephenson, A. (1976). Crustal remanence and the magnetic moment of Mercury. *Earth Planet. Sci. Lett*., **28**, 454–458.

Stevenson, D. J. (1987). Mercury's magnetic field: A thermoelectric dynamo? *Earth Planet. Sci. Lett*., **82**, 114–120.

Strom, R. G. (1979). Mercury: A post-Mariner 10 assessment. *Space Sci. Rev*., **24**, 3–70.

Strom, R. G., Trask, N. J. and Guest, J. E. (1975). Tectonism and volcanism on Mercury, *J. Geophys. Res*., **80**, 2478–2507.

Sundberg, T., Boardsen, S. A., Slavin, J. A., Anderson, B. J., Korth, H., Zurbuchen, T. H., Raines, J. M. and Solomon, S. C. (2012a). MESSENGER orbital observations of large-amplitude Kelvin-Helmholtz waves at Mercury's magnetopause. *J. Geophys. Res*., **117**, A04216, doi:10.1029/2011JA017268.

Sundberg, T., Slavin, J. A., Boardsen, S. A., Anderson, B. J., Korth, H., Ho, G. C., Schriver, D., Uritsky, V. M., Zurbuchen, T. H., Raines, J. M., Baker, D. N., Krimigis, S. M., McNutt, R. L., Jr. and Solomon, S. C. (2012b). MESSENGER observations of dipolarization events in Mercury's magnetotail. *J. Geophys. Res*., **117**, A00M03, doi:10.1029/2012JA017756.

Vilas, F. (1988). Surface composition of Mercury from reflectance spectrophotometry. In *Mercury*, ed. F. Vilas, C. R. Chapman and M. S. Matthews. Tucson, AZ: University of Arizona Press, pp. 59–76.

Vasavada, A. R., Paige, D. A. and Wood, S. E. (1999). Near-surface temperatures on Mercury and the Moon and the stability of polar ice deposits. *Icarus*, **141**, 179–193.

Vervack, R. J., Jr., McClintock, W. E., Killen, R. M., Sprague, A. L., Burger, M. H., Merkel, A. W. and Sarantos, M. (2011). MESSENGER searches for less abundant or weakly emitting species in Mercury's exosphere. Presented at 2011 Fall Meeting, American Geophysical Union, abstract P44A-02, San Francisco, CA, 5–9 December.

Watters, T. R., Head, J. W., Solomon, S. C., Robinson, M. S., Chapman, C. R., Denevi, B. W., Fassett, C. I., Murchie, S. L. and Strom, R. G. (2009a). Evolution of the Rembrandt impact basin on Mercury. *Science*, **324**, 618–621.

Watters, T. R., Solomon, S. C., Robinson, M. S., Head, J. W., André, S. L., Hauck, S. A., II and Murchie, S. L. (2009b). The tectonics of Mercury: The view after MESSENGER's first flyby. *Earth Planet. Sci. Lett*., **285**, 283–296.

Watters, T. R., Solomon, S. C., Klimczak, C., Freed, A. M., Head, J. W., Ernst, C. M., Blair, D. M., Goudge, T. A. and Byrne, P. K. (2012). Extension and contraction within volcanically buried impact craters and basins on Mercury. *Geology*, **40**, 1123–1126.

Weidenschilling, S. J. (1978). Iron/silicate fractionation and the origin of Mercury. *Icarus*, **35**, 99–111.

Weidenschilling, S. J. (1998), Mercury's polar radar anomalies: Ice and/or cold rock? *Lunar Planet. Sci.*, **29**, abstract 1278.

Weider, S. Z., Nittler, L. R., Starr, R. D., McCoy, T. J., Stockstill-Cahill, K. R., Byrne, P. K., Denevi, B. W., Head, J. W. and Solomon, S. C. (2012). Chemical heterogeneity on Mercury's surface revealed by the MESSENGER X-Ray Spectrometer. *J. Geophys. Res*., **117**, E00L05, doi:10.1029/2012JE004153.

Weider, S. Z., Nittler, L. R., Starr, R. D., McCoy, T. J. and Solomon, S. C. (2014). Variations in the abundance of iron on Mercury's surface from MESSENGER X-Ray Spectrometer observations. *Icarus*, **235**, 170–186.

Weider, S. Z., Nittler, L. R., Starr, R. D., Crapster-Pregont, E. J., Peplowski, P. N., Denevi, B. W., Head, J. W., Byrne, P. K., Hauck, S. A., II, Ebel, D. S. and S. C. Solomon (2015). Evidence of geochemical terranes on Mercury: Global mapping of major elements with MESSENGER's X-Ray Spectrometer. *Earth Planet. Sci. Lett*., **416**, 109–120.

Weider, S. Z., Nittler, L. R., Murchie, S. L., Peplowski, P. N., McCoy, T. J., Kerber, L., Klimczak, C., Ernst, C. M., Goudge, T. A., Starr, R. D., Izenberg, N. R., Klima, R. L. and S. C. Solomon (2016). Evidence from MESSENGER for sulfur- and carbon-driven explosive volcanism on Mercury. *Geophys. Res. Lett*., **43**, 3653–3661.

Wetherill, G. W. (1988). Accumulation of Mercury from planetesimals. In *Mercury*, ed. F. Vilas, C. R. Chapman and M. S. Matthews. Tucson, AZ: University of Arizona Press, pp. 670–691.

Whitten, J. L., Head, J. W., Denevi, B. W. and Solomon, S. C. (2014). Intercrater plains on Mercury: Insight into unit definition, characterization, and origin from MESSENGER datasets. *Icarus*, **241**, 97–113.

Wilhelms, D. E. (1976). Mercurian volcanism questioned. *Icarus*, **28**, 551–558.

Winslow, R. M., Johnson, C. L., Anderson, B. J., Korth, H., Slavin, J. A., Purucker, M. E. and Solomon, S. C. (2012). Observations of Mercury's northern cusp region with MESSENGER's Magnetometer. *Geophys. Res. Lett*., **39**, L08112, doi:10.1029/2012GL051472.

Zuber, M. T., Aharonson, O., Aurnou, J. M., Cheng, A. F., Hauck, S. A., II, Heimpel, M. H., Neumann, G. A., Peale, S. J., Phillips, R. J., Smith, D. E., Solomon, S. C. and Stanley, S. (2007). The geophysics of Mercury: Current status and anticipated insights from the MESSENGER mission. *Space Sci. Rev*., **131**, 105–132.

Zuber, M. T., Smith, D. E., Phillips, R. J., Solomon, S. C., Neumann, G. A., Hauck, S. A., II, Peale, S. J., Barnouin, O. S., Head, J. W., Johnson, C. L., Lemoine, F. G., Mazarico, E., Sun, X., Torrence, M. H., Freed, A. M., Klimczak, C., Margot, J.-L., Oberst, J., Perry, M. E., McNutt, R. L., Jr., Balcerski, J. A., Michel, N., Talpe, M. J. and Yang, D. (2012). Topography of the northern hemisphere of Mercury from MESSENGER laser altimetry. *Science*, **336**, 217–221.

Zurbuchen, T. H., Raines, J. M., Slavin, J. A., Gershman, D. J., Gilbert, J. A., Gloeckler, G., Anderson, B. J., Baker, D. N., Korth, H., Krimigis, S. M., Sarantos, M., Schriver, D., McNutt, R. L., Jr. and S. C. Solomon, S. C. (2011). MESSENGER observations of the spatial distribution of planetary ions near Mercury. *Science*, **333**, 1862–1865.